

# Advances in Inkjet-Printed Solid Oxide Fuel Cells

Leila Zouridi, Ioannis Garagounis, Anastasios Vourros, George E. Marnellos, and Vassilios Binas\*

Solid oxide fuel cells (SOFCs) are high temperature galvanic devices able to electrochemically convert chemical energy of fuels to electrical energy at remarkably high efficiencies. However, several challenges, associated with the complexity, scalability, and cost of the current fabrication processes, remain to be resolved for their large-scale deployment. Additive Manufacturing (AM) methods are proposed to address such fabrication-related issues, with Inkjet Printing (IJP) being one of the most promising. In this review, the use of IJP is examined as a potential AM method to deposit electrode and electrolyte thin films for SOFCs. The most important aspects of IJP for SOFCs fabrication processes, including ink formulation of active materials, inkjet deposition, printing optimization, and characterization of inkjet-printed thin films, are described in detail. Additionally, the effect on electrochemical performance of inkjet-printed SOFCs highlights the overall potential of this fabrication technique. Challenges and opportunities for the future development of the topic are also discussed.

## 1. Introduction

With energy demands increasing globally,<sup>[1]</sup> the prevention of an upcoming energy crisis has been established as a crucial challenge of our era.<sup>[2]</sup> While fossil fuels still constitute the primary

energy source used in conventional power generation thermal cycles, many concerns have been raised regarding their impact on climate change and the environment,<sup>[3–5]</sup> along with the fact that their natural reservoirs are finite.<sup>[6]</sup> In this context, new green directives and policies are being proposed and implemented in the global economy, such as in the case of the “Paris Agreement” agenda, the “European Green Deal” strategy and the “Climate Change 2021: Summary for Policymakers” guide recently published by the Intergovernmental Panel on Climate Change.<sup>[7–9]</sup> Thus, to successfully meet these challenging targets of clean energy transition, scientific research is urgently pursuing the development of more efficient and sustainable energy conversion approaches.

Solid oxide fuel cells (SOFCs) are considered as such promising energy conversion devices, due to their many advantages over conventional power generation systems. These include a) higher combined electrical and thermal efficiency (since fuel cell operation is not restricted by the thermodynamic limitations of classical thermal engines), b) higher energy density, and c) higher flexibility in operation and in fuel feedstock selection (from hydrogen to syngas, methane, ammonia or other fossil or bio-based liquid hydrocarbons and solid carbonaceous fuels), which result in low emissions per generated kWh<sub>el</sub>. Their technological compatibility with existing infrastructure and the innate robustness due to their compact design further increase their attractiveness.<sup>[10,11]</sup>

SOFCs are electrochemical galvanic cells where the chemical energy of a fuel through its spontaneous electro-oxidation reaction is directly converted to electrical energy. The basic components of an oxygen ion conducting SOFC, as in all electrochemical cells, are the dense ceramic solid electrolyte, which is sandwiched between two porous and conductive layers; the anode (fuel electrode) and the cathode (air electrode). The electrodes are electronically connected through a current collection system to support the electron flow from the anode to the cathode, comprising metal wires and interconnects when multiple unit cells are combined in an SOFC stack. The operating principle of an SOFC device involves the oxygen reduction reaction (ORR) at the air/oxygen exposed cathode, where molecular oxygen is converted to oxide ions, O<sup>2-</sup>, at the cathode/electrolyte interface, which are then transported through the dense ceramic ionic conductor (solid electrolyte) to the anode three phase boundary (TPB) and electrochemically oxidizes the fuel. As can be seen in **Figure 1**, the overall reaction taking place in

L. Zouridi

Department of Materials Science and Technology  
University of Crete  
Heraklion 70013, Greece

L. Zouridi, V. Binas

Institute of Electronic Structure and Laser – Foundation  
for Research and Technology Hellas  
Heraklion 70013, Greece  
E-mail: binasbill@iesl.forth.gr

I. Garagounis, A. Vourros

Department of Chemical Engineering  
Aristotle University of Thessaloniki  
Thessaloniki 54124, Greece

I. Garagounis, A. Vourros, G. E. Marnellos  
Chemical Process and Energy Resources Institute  
Centre for Research & Technology Hellas  
Thessaloniki 57001, Greece

G. E. Marnellos

Department of Mechanical Engineering  
University of Western Macedonia  
Kozani 50100, Greece

V. Binas

Department of Physics  
University of Crete  
Heraklion 70013, Greece

 The ORCID identification number(s) for the author(s) of this article can be found under <https://doi.org/10.1002/admt.202101491>.

DOI: 10.1002/admt.202101491

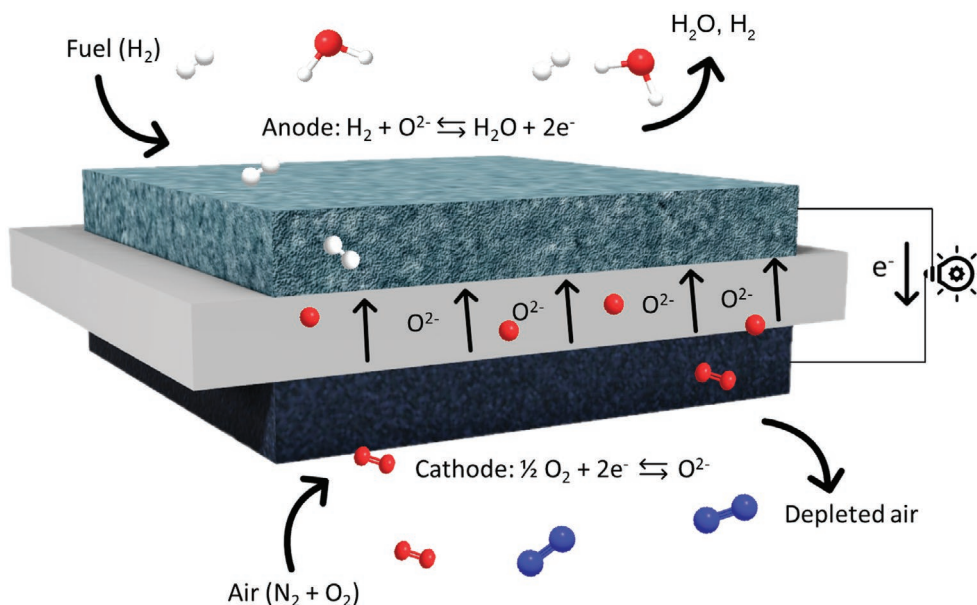


Figure 1. Operation principle of SOFCs.

an SOFC fed with hydrogen fuel is the sum of the two half-cell electrochemical reactions; water formation from its constituents, whose negative  $\Delta G$  is converted to electrical energy by the spontaneous flow of electrons through the external circuit.<sup>[12,13]</sup>

Notable worldwide demonstrations of SOFCs are mostly in medium power generation systems of tens to hundreds of kW scale, including pilot efforts funded in the USA,<sup>[14]</sup> the EU<sup>[15]</sup> (Norway,<sup>[16]</sup> UK,<sup>[17]</sup> Finland,<sup>[18]</sup> and Italy<sup>[19,20]</sup>), and Asia (Japan<sup>[21]</sup>), as well as other pilot projects such as auxiliary power units for heavy duty trucks.<sup>[22]</sup> Despite the success of such medium-scale and public-funded deployments, the market rollout and application of SOFCs at larger scales is still very low and far from reaching the desired economies of scale to substantially reduce the current high capital expenditure of SOFC cells, stacks, and systems. This can be attributed mostly to the scalability and complexity issues present in the currently employed manufacturing methods for SOFC cells and stacks, which are complex, time-consuming, and costly generating, at the same time, high quantities of waste material.<sup>[23]</sup> Thus, the development and implementation of less complex, scalable, and high precision methods of additive manufacturing (AM) for SOFC fabrication has attracted the interest of many research groups, in an effort to accelerate their wider applicability and market roll out on a global scale.<sup>[24–26]</sup>

## 2. Active Materials of SOFCs

SOFCs comprise a dense oxygen ion-conductive solid oxide ceramic electrolyte layer and two porous electron- and oxygen ion-conductive metal oxide electrodes. The production of electricity is achieved by the electrochemical oxidation of a fuel at the anode electrode, using oxygen ions formed by the reduction of oxygen molecules at the cathode electrode.<sup>[12,13]</sup> How-

ever, since these three different elements form a continuous cell assembly, it is recommended for all three counterparts to exhibit chemical and thermal compatibility, along with mechanical stability, especially for high temperature operation.<sup>[27]</sup> This section is devoted to a brief overview of conventional materials used in AM fabrication of SOFCs, grouped according to the component they are typically used for.

### 2.1. Electrolyte Materials

The main component of an oxygen ion conducting SOFC is the dense solid oxide ceramic electrolyte layer, which is an electron insulator and is required to display high unipolar oxide ion-conductivity ( $\text{O}^{2-}$ ), mechanical and thermal stability, as well as chemical compatibility with the neighboring electrodes.<sup>[11,28]</sup> The electrolyte layer as the main source of ohmic overpotential has to be adequately thin to allow high current densities at low overpotentials and thus high electrochemical performance.

Zirconium oxide is one of the most studied solid state electrolyte ceramic materials. It appears in three crystalline phases, all closely related to the cubic fluorite ( $\text{CaF}_2$ ) structure, and it consists of seven-coordinate zirconium centers. Below 1000 °C, it naturally forms a cubic monoclinic crystalline structure, then above 1000 °C it reorganizes to a tetragonal structure, while above 2300 °C concludes to a cubic structure.<sup>[29]</sup> However, this thermally induced crystalline transition constitutes an important drawback in zirconia layer manufacturing with thermal annealing due to the large volume change involved, which can possibly cause cracks during the cooling steps of the process. Additionally, zirconia tends to gradually reduce in air, while it may also deviate from its ideal stoichiometry when it is employed at high temperatures. Thus, modified zirconia-based ceramics are usually utilized in a stabilized cubic form, which

is usually achieved by adding metal oxides, such as CaO, MgO, Sc<sub>2</sub>O<sub>3</sub>, and Y<sub>2</sub>O<sub>3</sub>, to zirconia.<sup>[30,31]</sup> Interestingly, in the combined crystal structure with Y<sub>2</sub>O<sub>3</sub> doping (8 mol%), referred to as yttria-stabilized zirconia (YSZ), an increase in the concentration of oxygen vacancies is observed which results in the enhancing of the oxygen ionic conductivity to about 0.02 S m<sup>-1</sup> at 800 °C and 0.1 S cm<sup>-1</sup> at 1000 °C. Thus, it is considered to be the most appropriate candidate for use as the electrolyte material in the manufacturing of high operating temperature SOFCs (HT-SOFCs).<sup>[11,27,32]</sup>

In the case of intermediate temperature (IT-SOFCs), and low operating temperature SOFCs (LT-SOFCs), other materials such as gadolinium-doped ceria (GDC), samarium-doped ceria (SDC), and scandia ceria-stabilized zirconia (ScCeSZ) are more commonly implemented.<sup>[32–34]</sup> Ceria possesses a cubic fluorite crystalline structure and, similarly to zirconia, by the partial substitution of cerium cations with trivalent ions more oxygen vacancies can be introduced in the crystal structure of the mixed oxide, enhancing the ionic conductivity of the electrolyte. Doping with gadolinium or samarium results in an oxide ion conductivity of up to 0.005 S cm<sup>-1</sup> at 500 °C.<sup>[35]</sup>

## 2.2. Active Anode Materials

The solid anode porous layer of an SOFC functions as the catalyst where the electro-oxidation of the fuel takes place concurrently with the conduction and release of electrons, and should sufficiently fulfill both roles in order to exhibit lower activation and concentration overpotentials, attributed to charge and mass transfer limitations, respectively. Thus, the anode layers should consist of a material with high electrocatalytic activity for the hydrogen oxidation reaction or in general fuel electro-oxidation, high mixed electronic and ionic conductivity in order to achieve an extended active electrochemical zone, chemical compatibility, thermal stability, and high porosity with fine particle size.<sup>[11,28]</sup> According to the literature, such materials are nickel–YSZ composites or cermets (Ni–YSZ), lanthanum chromites or lanthanum titanate mixed oxides with perovskite structure such as La<sub>0.75</sub>Sr<sub>0.25</sub>Cr<sub>0.5</sub>Mn<sub>0.5</sub>O<sub>3</sub>, La<sub>0.8</sub>Sr<sub>0.2</sub>Cr<sub>0.97</sub>V<sub>0.03</sub>O<sub>3</sub>, or La<sub>0.4</sub>Sr<sub>0.6</sub>TiO<sub>3</sub>, composites of GDC such as Cu–GDC, Ni–NiO–GDC or mixtures of the two, and others currently under development.<sup>[36]</sup> The first, Ni–YSZ cermet, is commonly employed as an anode material in HT-SOFCs, while the latter are explored for their use in IT-SOFCs and LT-SOFCs.

Nickel(II) oxide, NiO, is the main oxide of nickel, with a face centered cubic crystalline structure, mostly studied for its p-type semiconducting properties in the field of sensors,<sup>[37,38]</sup> as an anode layer for electrochemistry applications (like batteries, supercapacitors,<sup>[39]</sup> and solid oxide fuel cells<sup>[40]</sup>) and as an anodic electrochromic material for chromogenic devices.<sup>[41]</sup> For use in SOFCs as an anode layer, NiO is mixed with YSZ or GDC resulting in nickel-based electrode composites.<sup>[40–42]</sup> Prior to operation, NiO has to be transformed to the catalytically active metallic phase, Ni, which is achieved by exposing the electrode in a reducing atmosphere under specified thermal protocols. The mixing of nickel with YSZ enhances the overall conductivity of the anode layer, up to 1000 S cm<sup>-1</sup> at 850 °C for Ni–8YSZ and 400 S cm<sup>-1</sup> at 850 °C for Ni–GDC, while it also extends

the anode TPB and protects nickel particles from solid-state agglomeration during SOFC operation over time.<sup>[40,43,44]</sup> Since the agglomeration of nickel particles is a major cause of degradation, its inhibition is crucial for the long term stable performance of SOFCs using such anodes. In Ni–YSZ cermets there is adequate compatibility of physical properties between materials, such as crystal structure and thermal expansion coefficient. However, recent studies have suggested there is still room for improvement in SOFC anodic materials.<sup>[40,43]</sup>

## 2.3. Active Cathode Materials

The solid cathode layer of SOFCs should exhibit characteristics such as high porosity, mixed electron, and oxide ion-conductivity, stability in oxygen-rich atmospheres (air or pure oxygen) as well as electrocatalytic activity for the ORR. Cathodic materials used in SOFCs are most commonly lanthanum-based perovskite oxides such as Sr-doped lanthanum manganite (LSM), lanthanum strontium cobaltite (LSC) or lanthanum strontium cobalt ferrite (LSCF), cobalt-based oxides like gadolinium strontium cobaltite, samarium strontium cobaltite (SSC), and PrBa<sub>0.5</sub>Sr<sub>0.5</sub>Co<sub>1.5</sub>Fe<sub>0.5</sub>O<sub>5+δ</sub> (PBSCF).<sup>[45–48]</sup>

The most common and well-studied cathode materials for SOFCs fabrication, are perovskite-type metal oxides. Perovskites have a general formula of ABO<sub>3</sub>, in which A and B are cations with a total charge of +6. The lower valence A cations (such as La, Sr, Ca, Pr, etc.) are larger and coordinated to 12 oxygen anions, while the B cations (such as Ti, Cr, Ni, Fe, Co, Zr, etc.) occupy a much smaller space and are coordinated to six oxygen anions. Full or partial substitution of A or B cations with cations of different valence is possible.<sup>[49]</sup>

LaMnO<sub>3</sub> (LMO) is an intrinsic p-type conductor, which upon doping with strontium or calcium cations exhibits enhanced electronic conductivity.<sup>[45]</sup> For *x* values of about 0.1 to 0.2, La<sub>1-x</sub>Sr<sub>x</sub>MnO<sub>3</sub> (LSM) exhibits high electrical conductivity and good mechanical and chemical stability at operating temperatures of HT-SOFCs, while a maximum conductivity value of up to 485 S cm<sup>-1</sup> at 1000 °C, for *x* = 0.5, has been also reported.<sup>[11]</sup> Unfortunately, LSM is a poor ionic conductor so, in order to overcome this issue, YSZ is usually mixed with LSM forming a composite cathode layer, conducting both electrons and oxide ions. As in the case of Ni–YSZ, in LSM–YSZ there is adequate compatibility of physical properties between the two materials, such as crystal structure and thermal expansion coefficient, thus making the LSM–YSZ layer mechanically stable at the elevated operating temperatures of HT-SOFCs.<sup>[27,45]</sup>

Materials considered for IT-SOFCs and LT-SOFCs cathode layer fabrication are the aforementioned LSCF, SSC, and PBSCF perovskites. These can be mixed with the electrolyte material to form composites with better thermal-compatibility with the electrolyte layer and, consequently, lower electrode polarization resistance.<sup>[50–53]</sup>

## 2.4. Cell Configurations and Stack Designs for SOFCs

Various configurations and geometries of SOFC unit cells and stacks have been tested in literature and implemented

according to the specifications of the desired application. More specifically, the geometry of an SOFC single cell or stack can be either planar or tubular, as schematically represented in **Figure 2a,b** accordingly.<sup>[54]</sup> The tubular shape of the electrolyte (and electrodes) allows for higher operating pressures, which is not usually required in fuel cell operation, and thus this geometry is mostly used in other solid electrolyte applications, such as high temperature steam electrolysis or electrochemical compressors. By contrast, the planar geometry of SOFCs is less applicable for high pressures. However, it is easier to fabricate using a wide variety of conventional ceramic processing fabrication techniques, including screen printing, tape casting, etc. Another important advantage of the planar geometry is its amenability to scaling, ranging from several square millimeters in lab scale tests up to hundreds of square meters in SOFC stacks for large scale applications. Hence, the majority of works on SOFCs involves planar cells. A typical planar stack is comprised of multiple cells connected in electrical series by metal plates, called bipolar plates since they separate the cathode of one cell from the anode of the next cell, while carrying electrons from the latter to the former.

Additionally, different cell configurations can be produced depending on which of the SOFC elements provides the mechanical support for the cell and is therefore the thickest one.<sup>[55]</sup> Such configurations are presented in **Figure 2c**. Traditionally, the electrolyte was implemented as the supporting layer, with a thickness close to 1 mm, with more recent commercially available cells fabricated with an electrolyte thickness of 150–300  $\mu\text{m}$  (Fuelcellmaterials). However, this configuration results in SOFCs of comparatively large ohmic resistance, limiting the achieved electrochemical performance. This has led to the widespread adoption of electrode-supported configurations (either on anode or cathode), in the case of both planar and tubular geometries. This configuration allows for much thinner electrolyte layers on the order of a few micrometers, thus further enhancing the electrochemical performance of SOFCs. A different configuration developed to reduce the thickness of SOFCs, used only in planar cells so far, is to add a fourth layer to the cell to provide the mechanical support. This layer is usually metallic and, consequently, such cells are referred to as metal-supported. One of the main advantages provided by this setup is that all of the ceramic (or cermet) functional layers are much thinner than in either of the other configurations and, thus, the ohmic losses of the cell can be minimized. This can also lead to cheaper and more robust cells, since metals are usually better than ceramics in both these respects. Their main drawback is that this extra layer must also be thermally and chemically compatible with, at least, the electrode that is in close contact with the metallic support, which limits the range of usable materials.<sup>[56]</sup>

### 3. Inkjet Printing as a Fabrication Technique

Common fabrication methods of SOFCs consist of conventional ceramic processing techniques. Screen printing, tape casting, slip casting, slurry spraying, spray pyrolysis, dip coating, and various types of powder pressing, usually followed by either sintering and/or lamination, are some of the

implemented methods.<sup>[23,57,58]</sup> In addition to these, other recently deployed fabrication methods are plasma (thermal) spraying, pulsed laser deposition, electrophoretic deposition, chemical vapour deposition, and magnetron sputtering.<sup>[23,27,57]</sup> The former are more cost-effective, facile, and easy to scale up techniques but lack in precision, while the latter are more costly but have the ability to achieve controlled deposition, applied so far at smaller experimental scales. However, in all aforementioned cases the complexity is high and the scalability is challenging.

Recent trends in additive manufacturing have introduced other, more sophisticated 3d and 2d printing techniques in the field of electrode films deposition, such as stereolithography, digital light processing, extrusion-based printing, aerosol jet printing, and inkjet printing (IJP).<sup>[25,26,59–62]</sup> Contrary to the common fabrication methods, additive manufacturing techniques offer facile, scalable, automated, contact-less, mask-free, and high-precision fabrication of thin-film devices, with reduced waste. Based on the aforementioned advantages, the AM methods exhibit a better environmental performance compared to conventional ceramic processing techniques, and this has been clearly demonstrated in a recent study dealing with the life cycle assessment of SOFCs fabricated by 3D printing, where an  $\approx 95\%$  decrease in most of the environmental impact categories was revealed.<sup>[63]</sup> Moreover, the biggest environmental burden on 3D printing fabrication of SOFCs has been attributed to the material production, mostly on nickel and lanthanum elements used, which can be remediated in a 70% recyclability scenario and the implementation of a circular AM fabrication approach.<sup>[63]</sup>

In this section the motivation for using IJP technology for ceramic thin film deposition, along with some of its basic principles and the characteristics of inks are discussed. A schematic of the manufacturing process for a fully inkjet-printed SOFC unit cell is presented in **Figure 3**, highlighting the layer-by-layer deposition characteristic of AM.

#### 3.1. The Appeal of Inkjet Printing Technology

IJP is an attractive material deposition and patterning technology that has received significant attention in recent years. Interestingly, it has grown from printing of graphic patterns, or nonfunctional features, into a rapid prototyping manufacturing technique. Global scale reports recently estimated that the inkjet printing market (valued at USD 48.3 billion in 2019) is expected to register a compound annual growth rate of 7.0% to 10.18% in the period from 2020 to 2025.<sup>[64,65]</sup>

The main appeal of this technology lies in it being a noncontact, additive, patterning, and mask-less approach of material deposition. The direct writing attribute of IJP allows for deposition of versatile thin films, the geometrical features of which can be modified easily due to the use of computer-aided design. Other attractive features of this technology are the reduced material wastage, low cost, and scalability to large area manufacturing. Due to all these benefits, in addition to its simplicity and speed, IJP has been investigated widely for use in applications such as electronics, biotechnology, microelectromechanical systems, and devices.<sup>[66–69]</sup>

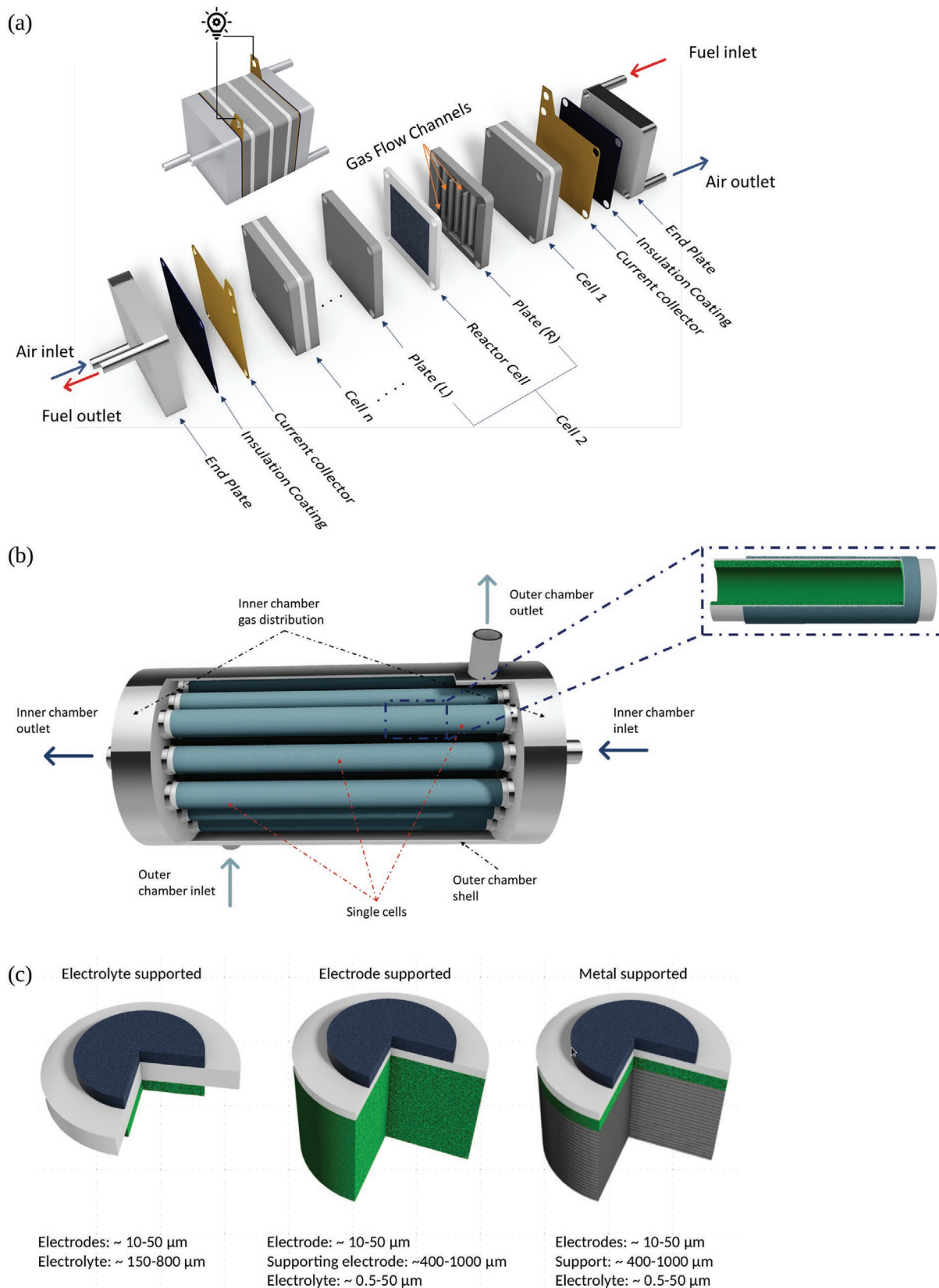


**Figure 2.** a) SOFC device design schematics. Planar geometry of an SOFC stack and its assembly. b) Tubular geometry of an SOFC stack, with cross-sectional view of a tubular single cell. c) SOFC configurations from left to right: electrolyte supported, electrode-supported, and metal-supported, with indicative thickness ranges next to each.

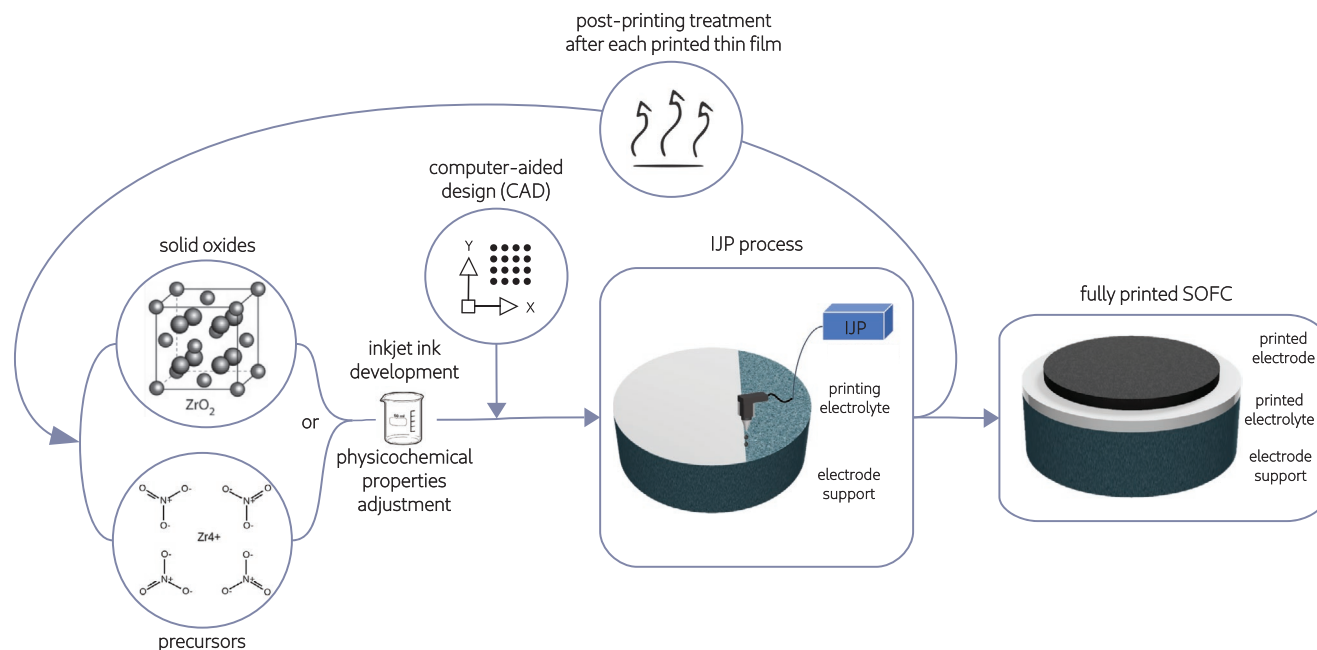


**Figure 3.** Schematic of the manufacturing process for a fully inkjet-printed solid oxide fuel cell (SOFC)

The implementation of IJP for thin film deposition opens new possibilities in device fabrication, however due to the novelty of this technique there are some limitations. In regards to the limitations intrinsic to the technique, inks used in IJP are required to be in a diluted liquid form of low viscosity, while a good dispersion of materials in the liquid medium without the presence of large agglomerates or high polydispersity is essential for optimal results (see Section 3.3). Additionally, since IJP is a layer-by-layer droplet-based deposition technique, it is largely applicable in the fabrication of 2D devices, and less so for 3D ones, as it is usually expected from additive manufacturing techniques. Most materials are compatible for deposition via IJP. Other nonintrinsic limitations of IJP are related to the novelty of the technique. Although IJP is well-established in some fields, such as patterning and coating, in others, such as nanomaterials thin film deposition, it has not been widely implemented so far.

Conventional methods of material layer deposition are better studied and implemented in large-scale fabrication. However, they have a number of limitations in terms of waste of excess material, restrictive processes due to usage of subtractive techniques, and an overall high processing cost. Such techniques usually require access to clean rooms, sophisticated equipment, and highly trained personnel to perform several time-consuming and relatively expensive micro- and nanomanufacturing procedures (e.g., lithography, oxidation, etching, and thin film deposition).<sup>[70]</sup> Additionally, in contrast to many conventional methods whose entire manufacturing procedure can take several days or weeks, inkjet printing is a well-established deposition technique that employs mostly inexpensive equipment and rapid postprocessing methods.

### 3.2. Basic Principles of Inkjet Printing

As a method, IJP basically achieves the accurate positional placement of picoliter volumes of fluid onto an arbitrary substrate. This definition encompasses a number of physical operations that both define and constrain IJP, such as the generation of droplets by the printhead, the positioning and interaction of droplets with the substrate, and the solidification mechanisms to produce a solid deposit.

#### 3.2.1. Generation of Droplets

Regarding droplets generation, this task is performed at the printhead of the inkjet printer either by a generation mechanism called continuous inkjet (CIJ) printing or by drop-on-demand (DOD). These different mechanisms correspond to two different printhead architectures.

In the CIJ printhead jetting architecture, a pressurized flow of ink is extruded by a nozzle, which breaks up midair to small droplets, by a piezoelectric transducer. The droplets then are either electrostatically charged, deflecting from their path, and collected in a gutter, or are left to land onto the substrate. In order for this method of drop generation to work, the ink needs to be conductive.<sup>[67,71]</sup> This, along with the fact that an ink collector/gutter is used and the ink needs to be recycled into the cartridge make this method messy and less versatile. Thus, the drop-on-demand model has dominated in both commercial and industrial inkjet printers alike.

In the DOD printhead jetting architecture, the drops are generated and extracted from the nozzle on demand, rather than in a continuous mode, either by a thermal-driven or piezoelectric-driven pressure pulse. For the thermal-driven pressure pulse, a thermal printhead is required with a thin-film heater in the

fluid reservoir, generating a small bubble of vapor that will expand on demand by the heat, generating the required pressure for droplet formation and jetting on the nozzle. For the piezoelectric-driven pressure pulse, a piezoelectric printhead is required with a piezoelectric transducer, which will generate the pressure pulse by direct mechanical actuation.<sup>[67,71,72]</sup> Other types of DOD drop generation mechanisms exist, all of which follow the same underlying principle of the ink drops being generated by a pressure pulse in the ink reservoir, controlled by an electrical signal, thus emitting ink only when is needed for deposition.

All DOD drop generation mechanisms, may suffer from common jetting instability issues, such as formation of ink tails, deviations on jetting angle, formation of satellite drops and nozzle clogging during the printing process, as depicted in **Figure 4a**. These issues can lead to lower print fidelity and can usually be overcome by optimizing ink composition, frequent monitoring of nozzle performance and tuning printing

parameters such as jetting voltage and the drop generation waveform. The latter refers to the electrical signal used to produce the pressure pulse in the ink reservoir, in order to produce ink droplets in a controlled manner.

Drop generation in a DOD piezoelectric cartridge usually comprises three steps; the first is the piezoelectric element expansion, where a negative pressure is generated producing a pressure wave in the chamber, Figure 4b-i; next is the conservation of voltage, where the traveling pressure wave reaches the nozzle orifice and wave inversion takes place, Figure 4b-ii; the last is the piezoelectric element contraction, where propagation of the inverted pressure wave toward the nozzle results in drop generation, Figure 4b-iii.<sup>[73]</sup> These three steps are regulated by the voltage rising time, dwell time, and falling time of the voltage waveform, respectively, in a typical “trapezoidal” waveform, shown in Figure 4c.<sup>[71]</sup>

### 3.2.2. Deposition of Ink and Substrate Wetting

The positioning and interaction of generated droplets with the substrate, the physicochemical properties of both the substrate and ink, along with their interfacial hydrodynamics are crucially important for the printed output. Key aspects of these interactions are prevalent during the drop impact, spreading, and overall wetting of the substrate. Jetting properties of the droplet, like velocity and size, are regarded as of high impact. However, the fluid characteristics of each ink, such as the viscosity and the surface tension will also determine the droplet spreading and wetting of the substrate surface.<sup>[74]</sup> In **Figure 5a** various resulting morphologies of a liquid drop upon impact onto a dry surface are presented.<sup>[74]</sup>

More specifically, upon impact with the substrate each jetted droplet will dissipate its kinetic energy by spreading on the substrate surface. This spreading will be counteracted by surface tension related to inward cohesive forces and viscous dissipation, as shown in Figure 5b, while the droplet will assume a shape on the substrate in an optimal way to minimize its free energy.<sup>[67,75]</sup> In principle, spreading of a sessile drop on a solid surface will follow the Young's equation model (Equation (1))

$$\cos(\theta) = \frac{\gamma_{SA} - \gamma_{SL}}{\gamma_{LA}} \quad (1)$$

where  $\theta$  is the drop contact angle,  $\gamma_{S/A}$  is the surface tension in the solid–air interface,  $\gamma_{S/L}$  the surface tension in the solid–liquid interface, while  $\gamma_{L/A}$  is the liquid–air interface, depicted in Figure 5c.<sup>[76]</sup> However, in IJP other parameters should be considered as well. For instance, the nature of small droplets generated at the printhead, in the scale of few picoliters, are characterized by a high surface area to volume ratio. Additionally, it is standard practice to use surfactants in the composition of inkjet inks, in order to facilitate drop formation and jetting. This addition results in a time-dependent dynamic change in surface tension of a droplet, depending on its state and on the inward placement of surfactants. For instance, during jetting surfactant molecules in a satellite drop are mixed within the liquid phase, resulting in high surface tension, while in the case of a sessile deposited drop, where air-to-liquid and solid-to-liquid interactions occur, surfactants tend to move toward

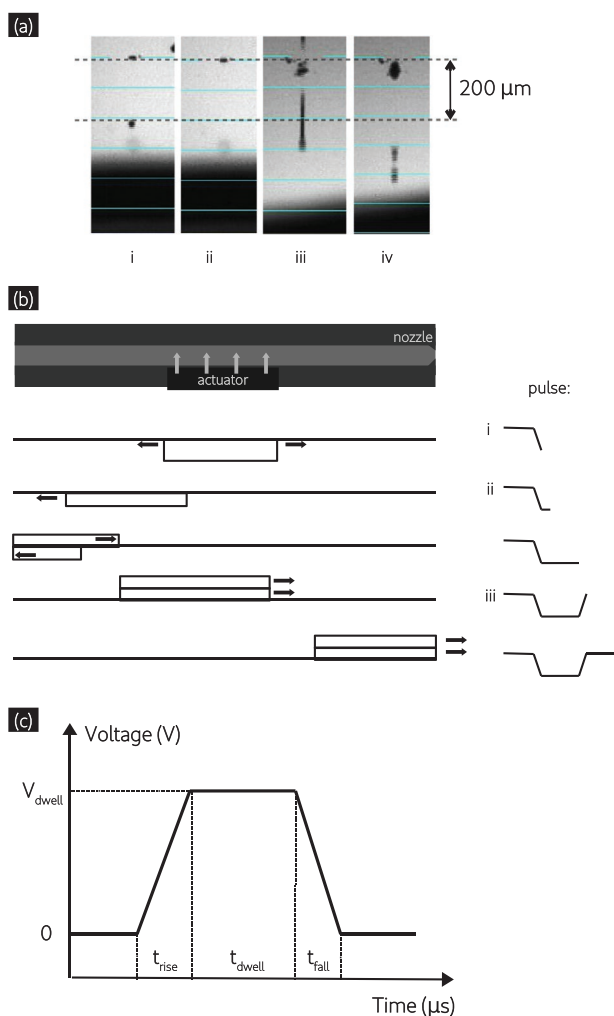


**Figure 4.** a) Images of drop generation examples using a Dimatix Inkjet Printer with (i) optimal drop formation, (ii) nozzle clogging, (iii) tail formation, and (iv) satellite drop formation. b) Schematic of drop generation in a DOD piezoelectric cartridge with stages of (i) negative, (ii) stable, and (iii) inverted pressure waves. c) Typical trapezoidal waveform with voltage and pulse width settings.

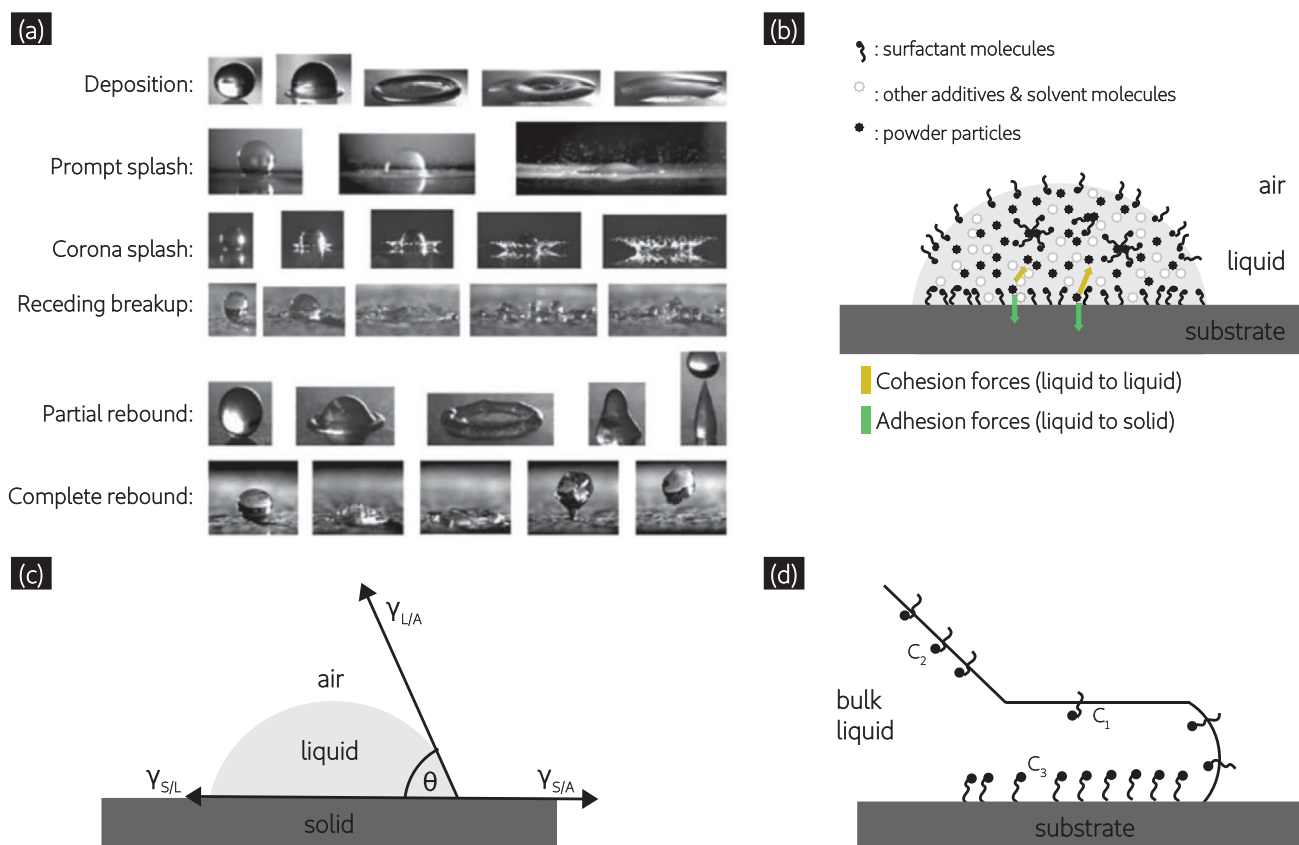


**Figure 5.** a) Various morphologies of liquid drops upon impact on a dry surface. Adapted with permission.<sup>[74]</sup> Copyright 2001, Begell House Inc. b) Illustration of an inkjet deposited drop containing powder particles, surfactants and other additives that interact with each other with cohesion forces in order to counteract the drop spreading caused by adhesion forces to the solid substrate. c) Illustration of a liquid inkjet drop on a solid substrate, with a contact angle as described by the Young's equation. d) Liquid film of ink with surfactants, wetting the substrate, with concentrations  $C_1 < C_2 < C_3$  of surfactant at the liquid–solid and liquid–air interfaces. Greater adsorption of surfactant molecules toward the interfaces leads to decreased surface tension values, in contrast to the bulk of the ink.

the interfaces (Figure 5d), decreasing the surface tension of the ink.<sup>[75]</sup>

Moreover, since most substrates are not ideally smooth surfaces, properties such as roughness, porosity, impermeability, wettability, and chemical composition of the substrate surface should be considered carefully.<sup>[77,78]</sup> Thus, treatment of substrates with rough or nonhomogeneous surface morphology is sometimes employed to optimize the wetting properties of the surface. This can be achieved by either wet chemical treatment, oxygen plasma treatment or other surface treatment techniques.<sup>[79]</sup>

### 3.2.3. Solidification of Droplets and Printed Films

In order to reach a uniform 2D pattern, adjacently deposited drops need to overlap, forming a coalescence region called “neck” (Figure 6a). The overall uniformity of prints is affected by the characteristics of the materials used and the selected printing parameters.

Concerning materials, uniformity of substrate surface, consistency of ink composition and individual drop flow during the spreading and drying steps are the most prevalent issues.

For example, a nonhomogeneous substrate or ink may perform poorly, producing inconsistent prints or uneven spreading of material and resulting in lower printing fidelity and repeatability. A porous substrate may inhibit spreading resulting in less overlap between drops, while a higher surfactant concentration may decrease the overall spreading time.<sup>[80]</sup> Monitoring the spreading of individual drops may facilitate printing procedures, by tuning ink composition in a way to induce a desirable behavior of deposited ink droplets when forming continuous liquid beads.

To this end, surface tension as an ink characteristic is of paramount importance, since its fluctuation during printing or the presence of surface tension gradients in drops during their spreading and drying may change their internal flow. Such changes in flow cause mass transfer, i.e., present molecules and particles move inside the drop and in the overlapping area of adjacent drops. Such phenomena are known as Marangoni (or Gibbs–Marangoni) effects and are well-studied in IJP, due to their impact on print uniformity.<sup>[66,81,82]</sup> When mass transfer occurs inside a deposited sessile drop, various effects have been observed on printed films, such as the displacement of solid particles during droplet drying, as shown in Figure 6b.

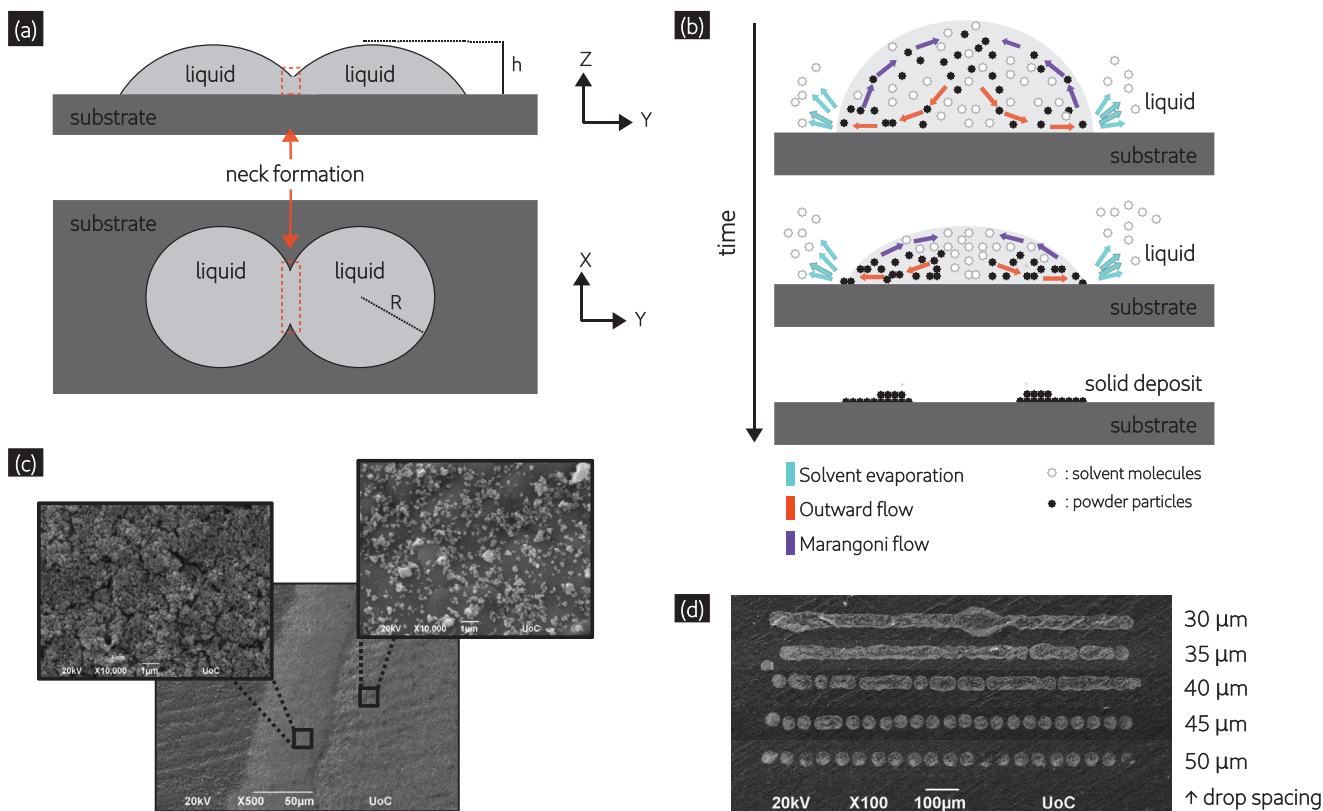


**Figure 6.** a) Side and top view of adjacent deposited drops coalescing, with highlighted neck formation. b) Schematic of a liquid ink droplet spreading and drying onto a solid surface. The resulting surface tension gradients produce outward flows and Marangoni flows, with solid particles migration and self-assembling toward the contact line of the droplet. c) Top view SEM image of the coffee stain effect on the contact line of a dried microliter droplet, with images of high particle concentration on the coffee stain area and lower particle concentration on the inner droplet area. d) Top view SEM images of inkjet printed lines with different drop spacing, affecting the overlap of adjacent drops.

A notable case is the coffee-stain effect, which takes place when a sessile drop, consisting of a volatile solvent, dries with a pinned constant circumference, rather than a constant contact angle.<sup>[83]</sup> These phenomena produce an outward flow of mass toward the drop perimeter, where particles accumulate and aggregate during drying, resulting in nonhomogeneous deposition, with areas of different concentration of particles. Moreover, solvent evaporation from the drop edge causes a surface tension gradient across the drop, resulting in an internal recirculating flow of particles from the lower surface tension areas of the drop edge toward the higher surface tension areas at the drop center.<sup>[84]</sup> The result is the characteristic coffee-ring shape upon droplet drying (Figure 6c).

Regarding printing parameters, drop spacing, print interval, drop size, and the use of substrate temperature are the most prevalent issues in the uniformity of prints. Drop spacing is a well-studied parameter, with a clear effect on print resolution, where small values result in excessive overlap of adjacent drops, while too large values result in insufficient overlap (Figure 6d).<sup>[71]</sup> Print interval and drop size may be used in relation to drop spacing in a way to optimize the dynamic interaction between the deposited liquid bead and the following incoming drop. The use of substrate temperature is usually implemented in order to accelerate solvent drying or

dewetting of deposited drops. This usually produces multiple results, from inducing thermal Marangoni flows in droplets and deposited liquid beads, to limiting the individual drops spreading, thus resulting in prints of smaller features and higher resolution.<sup>[67,71]</sup>

After the printing process, deposited films usually undergo some postprinting procedures, in order to form a solid, continuous and well adhered layer of the active material. Implemented methods are heavily dependent on the composition and type of material used, however the procedure usually aims at the removal of residual solvents and additives of the ink while fusing particles of the active material together. The sintering of particulate material can be achieved through various diffusion mechanisms, like surface diffusion, grain boundary diffusion, condensation–evaporation, and viscous flow.<sup>[85]</sup> In order to produce a solid printed layer various methods have been implemented, such as thermal sintering, rapid thermal processing, plasma sintering, photonic sintering, chemical sintering, spray drying, UV-curing/ozon surface treatment, microwave sintering, and other types of postprocessing treatments for coatings.<sup>[85,86]</sup>

Inkjet deposited layers can be mechanically tested for their durability, adhesion, bending and aging properties, along with chemical stability testing, depending on the requirements of the desired application.<sup>[69,87,88]</sup>

### 3.3. Physicochemical Properties and Performance of Inkjet Inks

To successfully address all the aforementioned issues (drop generation, substrate wetting, and film solidification) concerning ink development an “inkjet-printable” ink has to be formulated.

To evaluate drop generation and jettability of a potential inkjet ink, researchers calculate dimensionless numbers using the experimentally measured properties of such inks and then match the values of these numbers with the estimated optimal ranges from literature. More specifically, density ( $\rho$ ), dynamic viscosity ( $\eta$ ), and surface tension ( $\gamma$ ) of inkjet inks have been used to calculate the Ohnesorge,  $O_h$ , dimensionless number (Equation (2)), which is derived from the Reynolds,  $R_e$ , (Equation (3)) and Weber,  $W_e$ , (Equation (4)) numbers

$$O_h = \frac{\sqrt{W_e}}{R_e} = \frac{\eta}{(\gamma d)^2} \quad (2)$$

$$R_e = \frac{v \rho d}{\eta} \quad (3)$$

$$W_e = \frac{v^2 \rho d}{\sigma} \quad (4)$$

where  $d$  is the orifice diameter and  $v$  is the drop velocity.<sup>[89,90]</sup> In order to acquire a jettable ink the Ohnesorge number should lie between 0.1 and 1.<sup>[91]</sup> This usually corresponds to a typical range of properties for inkjet inks, with viscosity ranging from 5 to 25 mPa s and surface tension from 25 to 35 mN m<sup>-1</sup>. Another conventional use of the Ohnesorge number is by the value of its reciprocal, referred to as the  $Z$  value (Equation (5)). Thus, a typically jettable ink should display  $Z$  values between 1 and 10

$$1 \leq Z = O_h^{-1} \leq 10 \quad (5)$$

For optimal substrate wetting and drop spreading of an inkjet ink, researchers need to produce inks with lower surface tension than the surface energy of the substrate.<sup>[92]</sup> This can be quantitatively monitored by contact angle measurements of a sessile drop of ink on the substrate surface, which should be small, reflecting good wettability. However, if smaller features are to be printed as a way to increase printing resolution, an inkjet ink with a higher contact angle may be preferred in order to achieve lower wettability. It should also be noted that, using lower spreading inks to higher resolution may lead to increased ink consumption and thus higher manufacturing cost.

For uniformity of solidified films, researchers do use different techniques in regards to each specific issue. The use of viscous additives, or the use of mixtures of solvents with different boiling points have both been shown to minimize the coffee-ring effect in some cases.<sup>[82,93]</sup> In other cases, to achieve better surface homogeneity binder additives are employed to facilitate high particle density in deposited films. Facile solvent removal and faster postprocessing may be achieved when using volatile solvents in ink composition, however rapid evaporation of solvents may result in printing inconsistency.

For optimal long-term performance, inkjet inks should be tested for storage stability, i.e., keeping their physicochemical properties constant over time. Agglomeration of dispersed particles is a major concern for the ink formulation process, since it may result in ink inhomogeneity and irreversible precipitation of material. This can result in jettability issues, since it usually causes nozzle clogging, due to uncontrollable increase in particle diameter and high polydispersity. Thus, particle interactions should be kept to a minimum by utilizing particle shielding either with surfactants causing steric repulsion or ionic additives causing electrostatic repulsion.<sup>[94]</sup> Formulated inkjet inks should also keep their chemical as well as their physical composition constant, as long as needed for each specific application.

### 3.4. Chemical Composition and Types of Inkjet Inks

Inkjet inks can be formulated either by using the solid powders of active materials in a colloidal dispersion or a suspension, or by using a precursor liquid solution or slurry. The former is called *ex situ* or top-down formulation, since usually the commercially available micropowdered materials are purified/filtered or processed in order to reduce the particle size close to the nanoscale; whereas the latter is called *in situ* or bottom-up formulation, since precursor slurries of the active materials are used as-is in an inkjet printer.<sup>[95–97]</sup> A schematic of thin-film deposition using *ex situ*/suspension and *in situ*/precursor inkjet inks is presented in **Figure 7**.

*Ex situ* formulated inks are comprised of one or more liquid solvents (also called carrier solvents), the active material or pigment, and other additives to enhance ink stability and printability. These additives can be thickeners, surfactants, dispersing agents, wetting agents, adhesion promoters, antifoaming agents, humectants, substrate penetration promoters, curing agents, colorants, and other such chemicals commonly used in coating pastes and slurries fabrication.<sup>[67,98]</sup> All the components used for the composition of an *ex situ* ink other than the active dispersed powders comprise the “ink vehicle.” *Ex situ* inks are usually more prone to display nozzle clogging issues during the printing process due to the larger particle size of active materials. They are, however, more configurable than *in situ* inks due to their customizable composition by using different additives to optimize ink properties.

During formulation of inkjet-printable *ex situ*/suspension inks basic protocols from colloidal science are usually utilized for the stabilization and tuning of ink properties. For optimal long-term dispersion of colloidal systems two mechanisms widely used are electrostatic repulsion and electrosteric repulsion of suspended material. The aim of using such mechanisms is to create a repulsion between particles in solution, in order to prevent van der Waals interactions between them that would lead to rapid agglomeration and precipitation. When using the electrostatic mechanism, the charged surface of particles is the driving force of their repulsion. The charge can be either introduced by surface modification or pre-existing. It is usually employed when dispersed particles have a high dielectric constant or when using appropriate polar solvents with surfactants. To establish the optimal use of such additives, the

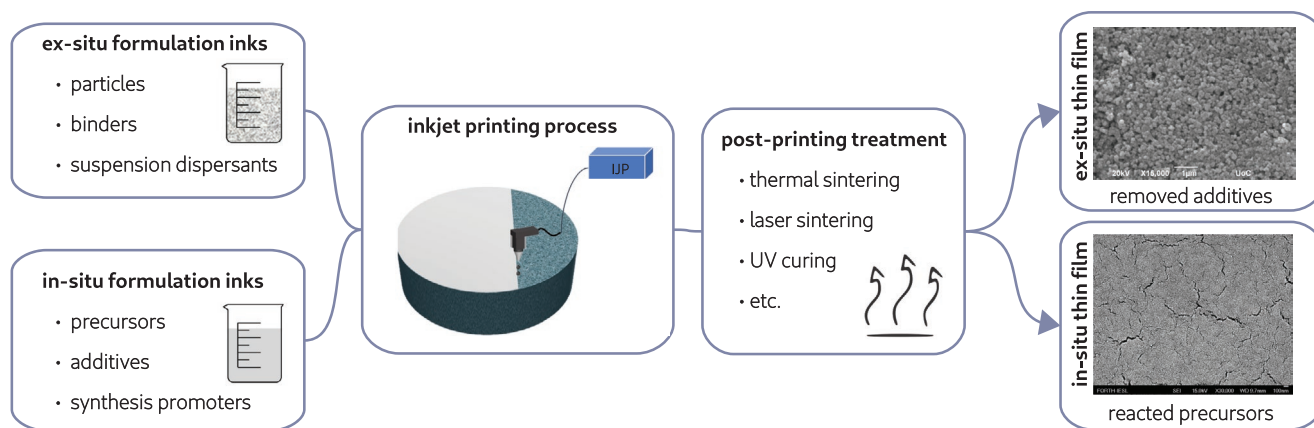


**Figure 7.** Schematic and SEM images of differences in thin film deposition between ex situ (suspension) and in situ (precursor) inkjet inks.

surface potential of particles should be monitored with zeta potential measurements for specific solvents and use of additives (salts, pH regulation, surfactants).

When using the electrosteric mechanism, steric repulsion between particles can be introduced by using additives with good affinity to the particle material to be absorbed on their surface. Steric forces are usually implemented by introducing appropriate polymer chains on the ink slurry or by chemically modifying the nanoparticles. This mechanism is optimal when using nonpolar solvents and for applications where surface modification of the material to be deposited is acceptable since it would require additional postprinting steps for the removal of polymeric additives and sintering of deposited particles. To establish the optimal use of such additives monitoring the dispersed particle size over time using particle size distribution measurements, such as dynamic light scattering, is crucial.

While such specific repulsion mechanisms are employed to prevent material aggregation, physicochemical properties described in Section 3.3, such as viscosity and surface tension, must be optimized accordingly since they have great impact on the stabilization of powder suspensions and on the ink printability as well. For example, due to the Brownian motion of suspended particles a low viscosity ink should be avoided during storage for better stability, however low viscosity (about few cP) is ideal for jetting performance. In this case, a common strategy to avoid sedimentation while maintaining printability is to use solvents that at room temperature display higher viscosity than at higher temperatures, which can be easily applied on the nozzles during printing. A second strategy is to non-Newtonian solvents with shear thinning properties, since during storage shear stress is lower than during jetting, thus making the ink more versatile. Another example, would be the modification of surface tension when using surfactants for stabilization, since surfactants tend to lower surface tension during drop formation or spreading, such as in the cases described in Section 3.2.3. Thus, the dynamic surface tension of inkjet-printable inks should be measured with every change in the formulation of inks.

In situ formulated inks can be comprised of solvents, precursors, reactants, reaction by-products, and nucleated crystal phases or even fully grown synthesized nanocrystals of active

materials, depending on the synthesis/formulation process. These chemicals can function in a dual role, as reactants and as additives in the formulated final ink, however the use of additives is usually limited in order to avoid any negative or unexpected effects on the synthesis reaction and nucleation process.<sup>[67,98]</sup> In situ inks usually are easier to print in regard to clogging issues, since the particle size of the active materials is already in the nanoscale. However, mass loading of in situ inks can be effectively lower producing less dense films. Additionally, printed layers may require more intense or multistep postprinting treatments, compared to layers printed with ex situ inks, especially when crystal growth is still ongoing.

In the case of in situ/precursor ink formulation, the methods for stabilization of ex situ inks apply in a great extend in the case of nucleated crystals. However, since the nucleation process can be ongoing, the conditions of ink storage, such as temperature and time should be controlled. For most in situ inks containing precursors, stabilization is not an issue, and optimizing of key physicochemical properties of inks should be performed by introducing thickeners for tuning viscosity and/or dilution of the precursor slurry by co-solvents for tuning surface tension.

Sections 4 and 5 are dedicated to the state-of-the-art on development of inkjet inks for SOFC fabrication. Recent original works will be presented. For simplicity, in situ and ex situ inks are discussed in separate sections.

#### 4. SOFC Advances with Ex Situ Inkjet Inks

In the research on SOFC materials printed by ex situ/suspension inks, there are a number of publications that focus on ink development and printing procedures, as well as on the obtained electrochemical performance. Since ink formulation is very flexible in ex situ inks, various ink compositions have been tested. A major differentiation between available publications lies in the choice of the main solvent as well as is the selection of the active material in use. Thus, this section will be divided in two sections related to the use of either water or organic solvents for the ink development of the various active materials (electrolyte, anode, and cathode materials).

#### 4.1. SOFCs From Water-Based Ex Situ Inks

Publications focusing on water-based formulation of ex situ inks, acknowledge the importance of water as an easily implemented, greener, safer and universal solvent. Its favorable properties such as high availability, low cost, minimal environmental impact, low toxicity, handling safety, neutral pH, and equipment compatibility, make water the ideal solvent in fabrication applications. However, in inkjet printing, a major drawback of water-based inks is the high surface tension of water,  $72.8 \text{ dynes cm}^{-1}$ , which is unsuitable for jetting.

In order to overcome this limitation, compatible surfactants are used to decrease the surface tension of the ink. This means that even in water-based inks organic molecules such as surfactants and other additives cannot be avoided. For instance, the use of surfactants in water-based inks may lead to issues with foaming, which is to be highly avoided in order to keep print fidelity; thus, antifoaming agents may be required to stabilize such inks. Moreover, the viscosity of water at room temperature is lower than the ideal, at  $1.0016 \text{ cP}$ , thus making the use of thickeners and secondary viscous solvents a common practice. Jetting with low viscosity water-based inks has been reported before, and is achievable, but with limited performance. Nonetheless, water-based inks are explored for SOFC fabrication with ink additives being the main focus of ink development as well as the main differentiation between literature studies.

Yashiro et al. reported on printing LSCF–GDC layers onto  $50 \text{ }\mu\text{m}$  GDC electrolyte substrates by utilizing a commercial single-nozzle inkjet printer (Pico Jet-1000, Microjet).<sup>[99]</sup> The water-based LSCF–GDC ink was developed by a multistep milling process, with a final solid loading of  $5 \text{ wt}\%$  cathode material. Water pH value was regulated at 10 by ammonia solution addition, while carboxylic acid ammonium salt copolymer dispersant was present at  $0.12 \text{ wt}\%$ . The mixing of LSCF and GDC powders occurred in consecutive milling steps, at a 57:43 final weight ratio of powders respectively. Particle size measurements of the ink revealed a sub-micrometer mean diameter distribution. The cathode films were deposited with up to 20 printing passes, and then thermally treated at  $1000 \text{ }^\circ\text{C}$  for 2 h, resulting in  $2 \text{ }\mu\text{m}$  to  $\approx 20 \text{ }\mu\text{m}$  thick layers.

Han et al. reported on the fabrication of SOFCs with LSCF inkjet-printed cathodes, by using a common HP printer.<sup>[100]</sup> Using only water as the solvent, along with commercial polymeric dispersing agent DISPERBYK-2012 and different quantities of 1,5-pentanediol as a surfactant and humectant, the authors printed LSCF cathode layers onto screen-printed YSZ electrolyte layers with a  $200 \text{ nm}$  GDC buffer layer. The formulated inks, as well as the as-obtained LSCF powders, were ball milled at  $110 \text{ rpm}$  for 36 h in order to break down agglomerates. Mean diameter measurements in inks with different surfactant concentration revealed that the presence of 1,5-pentanediol at  $20 \text{ wt}\%$ , allowed an optimal narrow particle size distribution at  $0.21 \text{ }\mu\text{m}$  mean diameter. Optimal inks were stable even after 34 days of storage, with no severe sedimentation reported. Printing parameters used were limited to the common desktop printer parameters, by changing the luminosity value of the software and with a fixed  $600 \times 300 \text{ dpi}$  resolution (Figure 8a). Printed layers were dried for 24 h and subsequently annealed in air at

$950 \text{ }^\circ\text{C}$  for 2 h. The optimal resulting layers were observed via SEM to exhibit an area porosity near  $13\%$  and  $5 \text{ }\mu\text{m}$  thickness.

In a later publication, the same group reported on the development of a similar ink composition using a dual-solvent system of  $80 \text{ wt}\%$  water and  $20 \text{ wt}\%$  ethanol, to print cathode (LSCF), composite cathode (LSCF–GDC) and electrolyte–cathode buffer (GDC) layers.<sup>[101]</sup> Inks were measured to exhibit Z values of about 10.6 (LSCF) and 11 (GDC), even after 17 days of storage, resulting from low viscosity values,  $\approx 2.5 \text{ cP}$ , and high surface tension values,  $\approx 36.5 \text{ mN m}^{-1}$  (Figure 8b). Mean diameter of dispersed particles was observed at  $0.27$  and  $0.17 \text{ }\mu\text{m}$ , for the two inks, respectively. To print the composite layer a tricolor cartridge was used with LSCF and GDC inks loaded in different color cartridges in order to print the composite by mixing the two color levels during printing. GDC buffer layers of  $900 \text{ nm}$  thickness were inkjet-printed onto  $10 \text{ }\mu\text{m}$  spin-coated YSZ electrolyte layer, while LSCF and LSCF–GDC cathode layers were printed onto the annealed buffer layers.

Most recently, the same authors used the same ink formulation to print a fully inkjet-printed anode-supported SOFC with the same HP Deskjet 1110 printer.<sup>[102]</sup> Water-based inks were developed to print the anode (NiO–YSZ), electrolyte (YSZ), and buffer (GDC) layers. In all three cases a mixture of water and ethanol was used to disperse the powders (4:1, 2:1, and 4:1 wt%, respectively), with the same dispersant, DISPERBYK-2012, and humectant, 1,5-pentanediol. In the case of the GDC buffer ink, polyvinylpyrrolidone (PVP)-K30 was additionally used as a binder. All the synthesized ceramic inks were ball-milled for 48 h at  $120 \text{ rpm}$  using 3, 5, and  $10 \text{ mm}$  zirconia beads. Inks were evaluated to be printable, with Z values of 8.69, 5.54, and 5.85, respectively. Printed NiO–YSZ and YSZ layers were cosintered at  $1400 \text{ }^\circ\text{C}$  for 3 h, while the printed GDC buffer layer was sintered at  $1200 \text{ }^\circ\text{C}$  for 2 h. The resulting layers were observed via SEM to exhibit adequate porosity, with a dense thin YSZ electrolyte. The thickness of the YSZ layer varied from  $0.4$  to  $2.5 \text{ }\mu\text{m}$  by changing the number of printed layers from one to five accordingly. The inkjet-printed SOFC with the  $0.8 \text{ }\mu\text{m}$  thick YSZ, achieved by two printing passes, was determined to be optimal in regards to the electrochemical performance (see Section 6). The cathode (PBSCF) layer was printed using an organic ex situ ink, which is discussed in Section 4.2 of this review.

The modification of a desk printer for SOFC fabrication was first published by Esposito et al. in 2015. They used a HP Deskjet 1000 and its black cartridge of  $600 \times 300 \text{ dpi}$  resolution to print YSZ layers using an ink with water-ethanol (4:1 volume ratio) as the solvent and a solid loading of 6 or  $20 \text{ wt}\%$  ( $0.9$  or  $3.7 \text{ vol}\%$ ).<sup>[103]</sup> Polymer thickener PVP was utilized at a  $53 \text{ wt}\%$  concentration in pure ethanol. A narrow particle size distribution, with a near  $100 \text{ nm}$  mean diameter, was achieved after mild milling on a rotational mill at  $100 \text{ rpm}$  for the span of 10 days. Dispersion stability was reported to be high with no precipitation even after 100 days of storage. Z values were calculated to be about 10.3 and 6.7 for the lower and higher solid loading inks, respectively, as presented in the graph in Figure 8c. YSZ electrolyte layers were printed onto Ni–YSZ substrates, in an anode-supported cell, followed by an annealing process at temperatures up to  $1300 \text{ }^\circ\text{C}$ , which resulted in dense

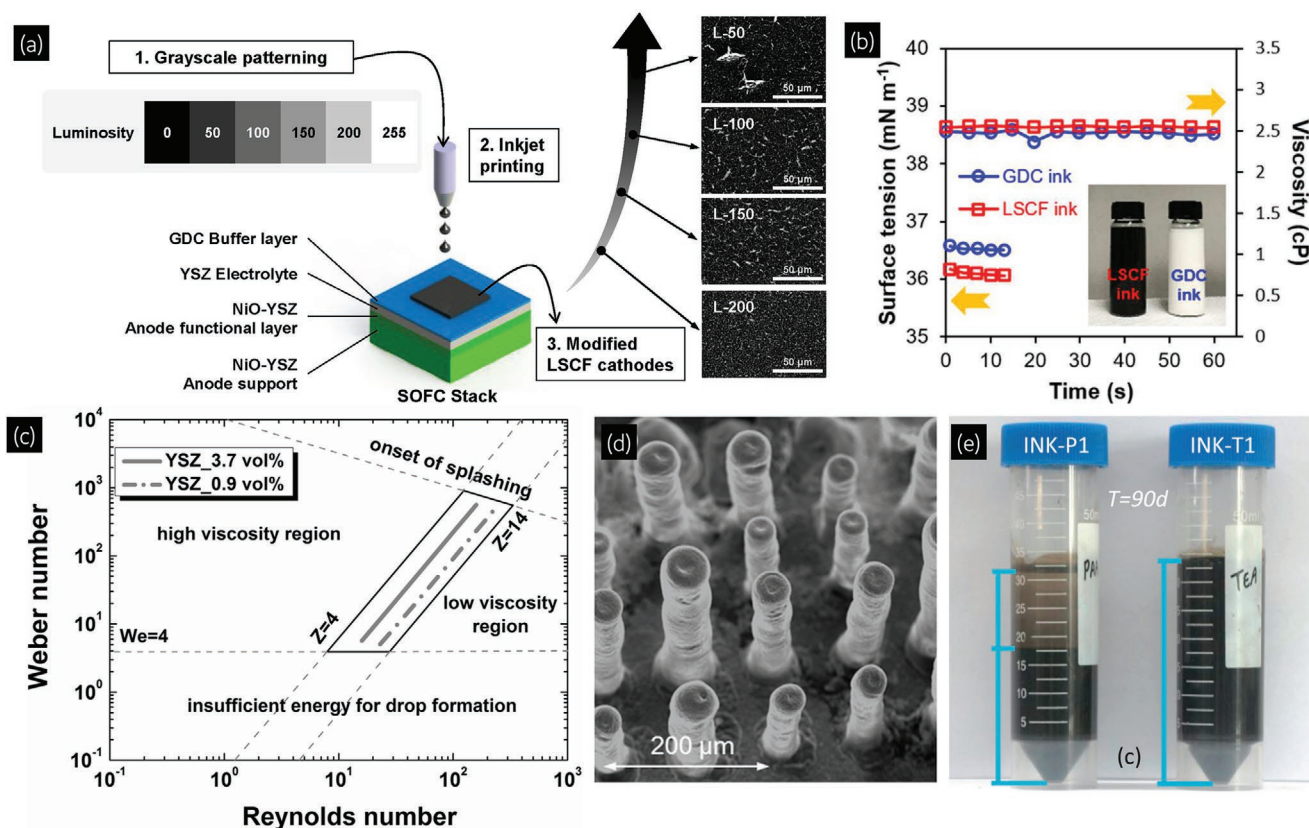


**Figure 8.** a) Schematic of the LSCF cathode fabrication using the inkjet printing method. Adapted with permission.<sup>[100]</sup> Copyright 2016, Elsevier. b) Surface tension and viscosity measurement results of the LSCF and GDC inks. Adapted with permission.<sup>[101]</sup> Copyright 2017, ACS. c) Weber–Reynolds numbers diagram of the regime for ink properties with good printability. Adapted with permission.<sup>[103]</sup> Copyright 2015, Elsevier. d) SEM images of YSZ pillars of 180 printed layers ( $\approx 300\ \mu\text{m}$ ) on Ni–YSZ substrate. Adapted with permission.<sup>[106]</sup> Copyright 2016, Elsevier. e) Photographs of sedimentation observations for INK-T1 and INK-P1 for 90 days storage. Adapted with permission.<sup>[108]</sup> Copyright 2018, Elsevier.

thin films of  $1.2\ \mu\text{m}$  thickness, which in the case of the high loading ink corresponded to five printing passes.

Li et al. reported in 2015 on the printing of YSZ electrolyte and SDC buffer layers, by using a modified commercial HP Deskjet 2668 equipped with a black ink cartridge (HP CC640ZZ 818).<sup>[104]</sup> Developed YSZ and SDC inks comprised of solvent water, 5 wt% polyethylene glycol PEG-4000 ( $M_w$ : 4000) thickener and 20 wt% commercial YSZ powders or 10 wt% SDC synthesized powders, respectively. Additionally, for the SDC buffer ink tri-ethanolamine (TEA) at 1 wt% was used as a dispersant. Calculated Z values of the YSZ and SDC inks were all in the jettable region, at 7.4 and 5.9, respectively, and displayed dispersion stability for up to five days of storage. An YSZ electrolyte layer and an SDC buffer layer was inkjet-printed onto a Ni–YSZ substrate, with five printing passes for the YSZ ink and two passes of the SDC ink, resulting in a dense and a porous layer of 75 and  $2\ \mu\text{m}$ , respectively. After printing, layers were thermally treated at  $1400\ ^\circ\text{C}$  for 5 h.

The same authors reported on printing SSC–SDC cathode layers, with a water-based ink containing 5 wt% of synthesized SSC and SDC powders in a 70:30 weight ratio.<sup>[105]</sup> PEG-4000 was again used at a 2.5 wt% concentration as thickener and pore former, along with additives glycerin and polyacrylic acid (PAA) at 1.25 and 0.75 wt%, respectively. After a milling process at 400 rpm for 1 h and treatment with an ultrasonic probe, a

uniform dispersion was achieved, and observed to be stable for up to three days with no apparent sedimentation. To study the effect of additional pore former in the resulting cathode layer, three distinct inks were utilized for printing, one with 10 wt% of PVP-K30 pore former, a second with 15 wt% PVP-K30 and a third with none. Cathode layers were printed with 45 printing passes onto an SDC buffer layer of an anode-supported substrate. The three distinct inks displayed very different results after thermal sintering, with the ink containing 15 wt% PVP pore former giving a noncontinuous film. By contrast, the layers printed with the ink without the additional pore former formed a thick layer with sintered particles and few pores, while the ones by the ink containing 10 wt% PVP, formed appropriately porous films of about  $15\ \mu\text{m}$  thickness.

In 2016, Farandos et al. reported on the printing of micro-structured 3D pillars of YSZ onto NiO–YSZ substrates, by utilizing a Ceradrop X-Serie piezoelectric inkjet printer equipped with a Dimatix printhead.<sup>[106]</sup> By using two commercially available YSZ powders of different particle sizes, development of water-based inks was accomplished with a solid loading from 3 to 24 wt%. Dispersion of powders was performed using an ultrasonic probe, followed by 24 h stirring process and mild centrifugation, resulting in stable dispersions of narrow particle size distribution, with a mean diameter of about  $110\ \text{nm}$ . PEG-35000 was utilized as a thickener at a 25 to  $40\ \text{mg}\ \text{cm}^{-3}$

concentration to adjust viscosity, while the alcohol ethoxylate Natsurf 265 at  $0.2 \text{ mg cm}^{-3}$  was added as a surface tension modifier. Resulting  $Z$  values of inks were all in the jettable region, with 4.4 to 9.2 calculated values. Printing of the 3D YSZ pillars was achieved by consecutive printing of either 50 or 180 layers with a high solid volume ink (24 wt% of YSZ) on Ni-YSZ substrates. An SEM observation of the printed YSZ pillars is presented in Figure 8d.

Two years later, the same authors reported on printing both YSZ and LSM-YSZ layers, using the same Ceradrop X-Series printer and Dimatix printhead.<sup>[107]</sup> For the YSZ ink, the formulation was the same as in their previous report, but with a solid loading of 19 wt%. The LSM-YSZ ink was formulated by mixing the YSZ and LSM water-based inks. Dispersion of LSM powders at 5 wt% in solvent water was achieved by sonication and mild centrifugation. Solvent water was pH-regulated at  $\text{pH} = 10$  by ammonium hydroxide addition, while the presence of dispersant “aluminum” at a final concentration of  $50 \text{ mg m}^{-2}$ , in regards to LSM particle surface area, ensured the stability of the dispersion. Again, PEG-35000 at a  $25 \text{ mg cm}^{-3}$  concentration and Natsurf 265 at  $0.2 \text{ mg cm}^{-3}$ , were added, to adjust viscosity and surface tension, respectively. Appropriate quantities of the YSZ and LSM dispersions were mixed in order to reach a final YSZ:LSM weight ratio of 4:6, with an LSM solid loading of 5 wt%. The  $Z$  value of the resulting composite ink was calculated to be 5.6, and was used to print cathode layers with 100 printing passes. Unfortunately, the resulting layers were repeatedly destroyed by the thermal treatment above  $550 \text{ }^\circ\text{C}$ , even after lowering the heating rate to  $1 \text{ }^\circ\text{C min}^{-1}$ . Additionally, by calculating and plotting the potential–pH diagram for the La–(Sr)–Mn– $\text{H}_2\text{O}$  system at 298 K, the authors noted that LSM tends to transform into lanthanum manganite in water solutions due to the high solubility of SrO, leading to the decomposition of the material. Ideally, to minimize this effect, they suggested regulation of pH in the range between 10 and 11. Interestingly, in the same region of  $\text{pH} > 9$ , the zeta potential of LSM was measured to be optimal, probably due to the resulting negative charge on the surface of particles, which in return induces dispersion stabilization via electrostatic repulsion.

The same year, Chen et al. published a study on the effect of two hydrophilic dispersants on the ink stability of LSCF water-based inks, in order to print cathode layers with a Fuji-Film Dimatix DMP 2850 inkjet printer.<sup>[108]</sup> Commercial LSCF powders were dispersed in water at 10 wt%, along with PEG-4000 at 5 wt%. Two additives were tested as dispersants, either PAA or TEA, at a 0.3 wt% concentration each. Ink dispersion was achieved by a mild milling step at 200 rpm for 24 h. Zeta potential measurements of the inks revealed greater potential values in acidic conditions, predicting better dispersion stability at lower pH values due to electrostatic repulsion of oxide surfaces. Indeed, after the addition of hydrochloric acid solution at  $0.1 \text{ mol L}^{-1}$  both inks displayed great dispersion stability, with the ink utilizing TEA remaining stable for up to 90 days of storage (Figure 8e). Resulting printed cathode layers were thermally treated via a multistep sintering process at a peak temperature of  $1000 \text{ }^\circ\text{C}$ . SEM observation revealed the layers to be smooth and uniform with no apparent cracks after sintering of the particles.

In their most recent work, published by the same authors, a similar study on stabilizing water-based inks to print layers of YSZ with the same FujiFilm Dimatix DMP 2850 inkjet printer, was elaborated.<sup>[109]</sup> Commercial YSZ ceramic powders were dispersed in water, in solid loadings up to 20 wt%, by utilizing an ultrasonic probe in order to break up agglomerated particles. Additionally, two types of dispersants were tested for their dispersion stability, either PAA for electrostatic stabilization of the ink, or polyacrylic acid ammonium ( $\text{PAANH}_4$ ) for electrosteric stabilization in different concentrations ranging from 0.25 to 2.00 wt%. From their analysis on the sedimentation ratio of inks after 72 h of storage,  $\text{PAANH}_4$  was revealed as the most effective, with minimal and reversible phase separation, kept to a minimum at an optimal concentration of 1.0 wt%, with a 20 wt% of YSZ solid loading. Glycerin (2 wt%) as a drying retardant and PEG-4000 (5 wt%) as a defoamer and surface tension regulator were added in order to enhance the overall printability. Finally, the ink was pH-regulated at  $\approx 7$ , by addition of  $0.1 \text{ mol L}^{-1}$  HCl and filtered with a 220 nm aperture filter to give a mean particle diameter of 208 nm, while the  $Z$  number was calculated to be 7.6 for the final ink.

The YSZ electrolyte layers were inkjet-printed onto a commercial NiO-YSZ anode substrate (SOFCMAN, China) with ten printing passes. Printhead voltage was regulated at 15 mV to attain good drop generation, without tail formation. The printed layers were treated by a multistep thermal drying and annealing in air, from  $50 \text{ }^\circ\text{C}$  up to  $1450 \text{ }^\circ\text{C}$ , the steps and rates of which were meticulously regulated based on TGA measurements of a sample of dried ink. SEM observations revealed no coffee-ring effect present, even in single deposited drops, while the adhesion of the final film was clear, with no evident delamination or cracks, and an average electrode layer thickness of  $3.5 \text{ } \mu\text{m}$ .

## 4.2. SOFCs From Organic Solvent-Based Ex Situ Inks

Organic ex situ inks are characterized by their flexibility and stable performance in IJP, which results in printed films of high print fidelity and high homogeneity. In the literature for development of inkjet inks, a common starting point is the use of previously studied and reported formulations for pastes or thick dispersions of the active materials. Such thick dispersions are utilized in other deposition techniques, such as screen printing, and by modifying the composition such formulations can be adjusted to IJP inks requirements. This is the case for most inkjet inks development, and SOFCs fabrication is no exception, with extended use of established organic solvents from pastes development.<sup>[58]</sup>

### 4.2.1. Single-Solvent Systems Based on $\alpha$ -terpineol

Many studies use  $\alpha$ -terpineol or a mixture of its isomers to produce inkjet-printable SOFC inks especially since its viscosity, and thus its rheological behavior, is easily tailored with temperature. Such is the work of Suresh et al., who in 2008 and 2009 published their results on inkjet printing of YSZ, NiO, and LSM powders using a FujiFilm Dimatix DMP 2831 inkjet

printer.<sup>[110–112]</sup> Solvent  $\alpha$ -terpineol was used to disperse the solids, at a maximum solid loading of 10.7 wt%, while polyvinyl butyral, butyl benzyl phthalate, and polyalkalyne glycol were used as binders and plasticizers. After 12 h of ball milling, they achieved stability of the ink, with a shelf-life of 2 to 3 weeks on average without irreversible precipitation. With this ink composition they printed the electrolyte (YSZ), anode interlayer (NiO–YSZ), cathode interlayer (LSM–YSZ), and cathode current collector (LSM) layers onto an NiO–YSZ anode–support as substrate. The main parameter tested during printing was the cartridge temperature, where 58 °C was reported to be optimal, while substrate temperature was set to 80 °C during printing and 100 °C or 120 °C during the intermediate drying between the printing of multiple layers.

Another such case is the conference proceeding publication of Faino et al. who, also using a FujiFilm Dimatix DMP 2831 inkjet printer, reported on the printing of NiO and YSZ powders.<sup>[113]</sup> Compared to the works of Sukeshini et al., powders were dispersed in  $\alpha$ -terpineol using a higher solid loading, close to 30 wt%. Additionally, various commercial dispersants were tested, with optimal results achieved with Lubrizol Solperse S13940. Finally, overnight milling was utilized in order to break down any solid powder agglomerates. A near 50 °C cartridge temperature was chosen to print the anode (NiO), the electrolyte (YSZ), and interconnect (lanthanum-doped strontium titanate) layers onto an yttria-stabilized zirconia substrate.

These early reports highlighted the need for additional research on ex situ SOFC inks for the optimization of ink composition. Thus, later reports seem to focus on a well-implemented formula used for screen-printed pastes, combining  $\alpha$ -terpineol with dispersant ethyl cellulose. More specifically, in their reports Hill et al. conducted an extensive study on the role of ethyl cellulose on the homogeneity of LSCF layers, printed with a FujiFilm Dimatix DMP 2831.<sup>[114–116]</sup> Various inks were prepared by dispersing LSCF powders in  $\alpha$ -terpineol in solid loadings ranging from 3.5 to 12 wt%, while the use of ethyl cellulose was kept to a minimum of 0.1 wt%. In order to break up any LSCF agglomerates, inks were ball-milled for a minimum of 1 week. Resulting layers were reported to display a distinct coffee-ring effect when printing with 0.1 wt% of ethyl cellulose, in contrast to the layers from inks without additives, where the coffee-ring effect was fairly minimal. This effect was enhanced by increasing the printing passes, forming a “volcano-like” elliptical microfeature on multiple passes as presented in **Figure 9a**. The authors proposed that such unique features observed with ethyl cellulose inks, could be exploited to promote a more performance-favorable electrode microstructure, e.g., to enhance porosity and gas diffusion in microfabricated solid oxide fuel cells ( $\mu$ -SOFCs).<sup>[115,116]</sup>

Similarly, in 2015 and 2017 Rahul et al. reported on the IJP of YSZ electrolyte layers, using a custom-made printer equipped with a DOD electromechanical Domino Macrojet printhead with nozzles of 90  $\mu\text{m}$  orifice diameter each, presented in

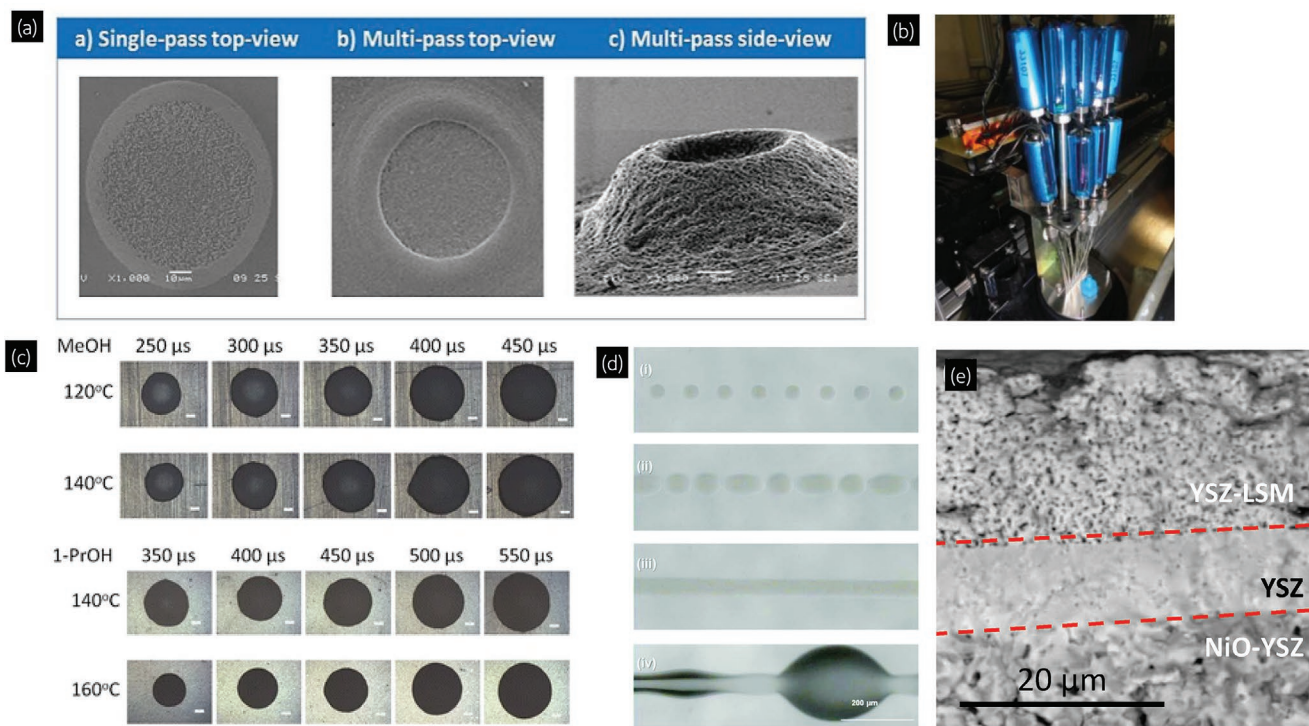


**Figure 9.** a) Top and side view SEM images of dots fabricated with ethyl cellulose containing ink. Adapted with permission.<sup>[116]</sup> Copyright 2016, Tech-Connect Briefs. b) Electromagnetic print head in DOD-IJP system (Domino, UK). Adapted with permission.<sup>[117]</sup> Copyright 2015, Springer. c) Drops deposited at different substrate temperatures and nozzle opening times for MeOH- and 1-PrOH-based inks. Adapted with permission.<sup>[127]</sup> Copyright 2015, Springer. d) Images of dot and line patterns formed by IJP of the tetradecane-based NiO ink using 100, 50, 35, and 25  $\mu\text{m}$  drop spacing. Adapted with permission.<sup>[132]</sup> Copyright 2016, RSC. e) Cross-section SEM images of the printed NiO-YSZ|YSZ|YSZ-LSM. Adapted with permission.<sup>[107]</sup> Copyright 2018, Elsevier.

Figure 9b.<sup>[117–119]</sup> YSZ powders were successfully dispersed in  $\alpha$ -terpineol, at a solid loading of about 20 wt% with 10 wt% of ethyl cellulose. A mild milling process, at an optimal 160 rpm for 4.5 h, was implemented in order to achieve an average particle size of 572 nm in the dispersion. Finally, the ink displayed a four-week long storage stability, and the electrolyte layer was printed onto either porous-alumina or metal substrates. Although the ethyl cellulose binder concentration was significantly higher than the formulations of Hill et al., no coffee-ring effect was reported on printed layers, even after multiple passes.

#### 4.2.2. Dual-Solvent Systems Based on $\alpha$ -terpineol

In their most recent publication, the same authors reported on inkjet printing of YSZ films, with the same ink composition, custom printer and similar printing parameters, onto stainless steel plates.<sup>[120]</sup> However, their previously optimized ink was diluted with an unspecified amount of ethanol solvent and ultrasonicated prior to printing. The practice of diluting dense or viscous inkjet-printable inks is a reoccurring trend in IJP, usually conducted to achieve better printability with lower printing temperatures. Apart from lowering the energy and system requirements of the manufacturing process, printing without applying temperature at the cartridge is sometimes necessary, as in the case of print-heads that support printing at room temperature exclusively, or with inks that are temperature-sensitive (see Section 5). Thus, a dual-solvent system can be implemented in ink development, by using two different miscible solvents. Nonetheless, a diluted *ex situ* ink implies a lower solid loading, which results in both less dense printed layers per printing pass, and usually limited dispersion stability with heavy sedimentation, due to lacking Stokes' drag frictional forces to impede Brownian motion of suspended particles.<sup>[94]</sup>

Diluting terpineol-based SOFC inkjet inks has been reported in various reports of Tomov and co-workers from 2010 to 2017.<sup>[121–130]</sup> In their publications,  $\alpha$ -terpineol and various primary alcohols are used as dual-solvent systems to form the ink vehicle, along with different binders. In their work, inkjet deposition is performed using a custom modified Domino Macrojet printer, equipped with an electromagnetically (EM) driven single-nozzle print-head of 100  $\mu\text{m}$  orifice with the ability to print at room temperature. In their 2012 report they achieved printing of GDC inks with 5 wt% solid loading and 0.5 wt% of binder ethyl cellulose.<sup>[122]</sup> The composed dual solvent system comprised of  $\alpha$ -terpineol and methanol, with varying solvent ratios from 70:30 to 20:80 vol%, respectively. Results revealed better ink stability, printability, and drop integrity in the case of the 50:50 vol% solvent ratio. Extensive wet milling of GDC powders before dispersing produced inks with a final dispersed particle size of 400 nm.

The same authors reported on printing YSZ inks of similar ink formulation, however bis(2-ethylhexyl) phthalate was used as an additional binder, while a higher solid loading of 15 wt% was examined along with the previously used 5wt%.<sup>[121,123]</sup> The viscosity of these inks was about 2–5 cP, even for the higher solid loading inks, making printing at room temperature possible, as

discussed at the beginning of this section. Since the EM single-nozzle print-head operates in a different manner than conventional piezoelectric DOD, instead of using a drop generation voltage waveform, the authors studied the effect of parameters such as jetting pressure and nozzle opening.

In their following publications, similar ink compositions were used to print anode layers with a mixture of NiO and GDC powders.<sup>[125–128]</sup> The ink vehicle comprised of a dual-solvent system with mixtures of  $\alpha$ -terpineol and primary alcohols, such as methanol, ethanol or 1-propanol, along with unspecified polymer binders. An optimization of the milling duration of inks revealed that a 10 h procedure can achieve a narrow sub-micrometer particle distribution in the case of methanol use as cosolvent.<sup>[125]</sup> Although the EM print-head was kept at room temperature, the authors studied the effect of substrate temperature on the resulting printed layers. Increasing the substrate temperature (in the range of 80 to 180 °C), decreased the single-drop diameter drastically, while minimizing the coffee-ring effect. This was the case for all alcohol co-solvents used, which are of lower boiling point than terpineol (Figure 9c). As predicted from theory, these experimental results revealed the impact of substrate temperature during the printing process. As a result of the increasing substrate temperature, a gradual evaporation of the solvents is taking place at the contact line of each printed droplet. As discussed previously in Section 3.2.3, these phenomena can create a surface tension gradient throughout the drop, which induces thermal Marangoni flows balancing the outward flow of the spreading drop, resulting in the reduction of the coffee-stain effect on printed drops at higher substrate temperatures.

More recently, Wang et al. reported on printing NiO–GDC cermet anode layers using  $\alpha$ -terpineol and methanol co-solvents in a 1:1 volume ratio, while dispersant hydroxy-propyl cellulose was added at a 2:100 weight ratio in regards to the active material used.<sup>[129]</sup> By processing the ink with an 8 h milling procedure, a mean dispersed particles diameter of about 400 nm was achieved. The NiO–GDC anode ink was printed onto commercial anode substrates, followed by the printing of an infiltrate GDC ink, of similar composition. This infiltrated electrolyte ink is used in order to improve the anode performance stability by reducing the nickel particle coarsening during SOFC operation, a well-studied issue of Ni-based anodes in fuel cells.<sup>[131]</sup>

In 2017 Tomov et al. reported on the dispersion of LSCF and GDC commercial powders in  $\alpha$ -terpineol and methanol, to formulate separate suspensions to be mixed into a single cathode composite ink.<sup>[130]</sup> Again, hydroxy-propyl cellulose was added in each individual ink to act as binder, as polymeric dispersant and as pore former to the printed layers. Each suspension was milled in a planetary ball mill and were measured to have a sub-micrometer mean particle size. The final composite ink, obtained by mixing LSCF and GDC suspensions at a 40:60 and 60:40 volume ratio, was printed by a custom Domino Macrojet printer, equipped with an EM print-head of 100  $\mu\text{m}$  nozzle orifice. Printed cathodes were then sintered in air at 1080 °C for 1.5 h, and then a procedure of GDC infiltration by printing with an *in situ* ink was performed. This process is further discussed in the “*in situ* inks” section of this review (see Section 5.1).

#### 4.2.3. Other Organic Single-Solvent Systems

Apart from using  $\alpha$ -terpineol as main organic solvent in ex situ inks, few reports of SOFC ink development with other single-solvent systems have been reported. In the case of Rho et al., the use of three solvents such as toluene, tetradecane or  $\alpha$ -terpineol, where tested on dispersing NiO powders with a solid loading around 12 wt%.<sup>[132]</sup> The Z values of resulting inks were calculated to be about 31, 8, and 0.6, respectively, for each solvent tested. As expected, stable drop generation at room temperature was achieved only with the tetradecane-based ink, using a FujiFilm Dimatix DMP 2831 inkjet printer. By tuning the drop spacing, the authors achieved optimal print fidelity at a drop spacing of 35  $\mu\text{m}$  (Figure 9d), while the resulting layers displayed uniformity in surface morphology.

In 2013, Deiner et al. published an in-depth study on the dispersing effect of different additives for the ink development of 10 wt% NiO dispersions in butanol.<sup>[133]</sup> A plethora of different additives were tested, such as lignoceric acid, oleic acid, glycerol trioleate, Menhaden fish oil, linoleic acid, linolenic acid, and stearic acid, at 0.4 wt% concentration. Formulated inks were roll-milled at 60 rpm for up to 3 weeks, and subsequently observed up to one week for sedimentation. Inks with either oleic acid, glycerol trioleate or linoleic acid displayed phase separation during the first day of storage. By contrast, inks with Menhaden fish oil, stearic acid, lignoceric acid, and linolenic acid displayed slightly better dispersion stability. Mean diameter of dispersed particles were in the sub-micrometer region for all formulated inks. Characterization of dried NiO powders after sedimentation by infrared spectroscopy was used to assess the mechanism of the surface bonding of each dispersant. The obtained results indicated that all dispersants displayed at least some chemisorption to the NiO surface, which implies that the poor dispersion stability observed is attributed to the low viscosity of inks rather than to the inefficiency of dispersants. Unfortunately, no IJP deposition of these dispersions was reported.

More recently, Farandos et al. published a work on the printing of LSM–YSZ cathodes, using a Ceradrop X-Serie piezoelectric inkjet printer, equipped with a Dimatix printhead.<sup>[107]</sup> By mixing two separately formulated dispersions of LSM and YSZ in butanol solvent, at a 60:40 solid ratio, an ink of final solid loading of 16 wt% was obtained. The resin polyvinyl butyral was utilized as a dispersant and plasticizer at a 14 mg mL<sup>-1</sup> concentration of the final LSM–YSZ ink. The Z value of the ink was calculated to be equal to 2.3, suitable for IJP. Thus, LSM–YSZ cathode layers were printed onto a previously inkjet-printed YSZ layer (Ni–YSZ anode-supported, see Section 4.1) at room temperature, resulting in a highly porous film of  $\approx 20 \mu\text{m}$  thickness. In Figure 9e, a cross-sectional SEM image of the printed NiO–YSZ|YSZ|YSZ–LSM single-cell after sintering at 1200 °C is presented, indicating the porosity and strong adhesion of the inkjet-printed cathode layer to the YSZ electrolyte.

In another recent publication, Kamlungua et al. reported on the inkjet printing of novel Ag-core/SDC-shell (Ag@SDC) nanoparticles as cathode layers, using a Fujifilm Dimatix Printer DMP-2831 with a DMC-11610 cartridge (10 pL nozzle size).<sup>[134]</sup> After hydrothermal synthesis of the core–shell nanoparticles (<60 nm), a one-step ex situ ink formulation was utilized

simply by dispersing the as-dried nanoparticles in ethylene glycol at a solid loading of 30 wt%. During IJP, drop generation was achieved with an applied voltage of 30–40 V, while no cartridge temperature was applied. Ag@SDC and plain Ag thin films were deposited on an SDC electrolyte substrate (7 printing passes, 30  $\mu\text{m}$  drop spacing, 60 °C substrate) and annealed in air at different temperatures from 300 to 800 °C for 48 h, in order to compare their thermal stabilities. FESEM observations revealed augmented thermal stability in the case of the Ag@SDC cathode, with no visible agglomeration or cracks up to 450 °C, and small cracks observed at 600 °C. On the contrary, the plain Ag film exhibited intense agglomeration and densification of the layer, as was expected from authors. However, an annealing temperature of 550 °C was used for the final samples, in order to remove any remaining organic residues from the synthesis of Ag@SDC nanoparticles. Stability measurements of the inkjet-printed cathode on YSZ single-crystal wafers (Pt|YSZ|Ag@SDC) was studied further by long-term electrochemical testing at 450 °C, which will be discussed later on in Section 6.

As mentioned in Section 4.1 on “water-based ex situ inks,” in a recent publication. Han et al. reported on a fully inkjet-printed SOFC unit cell using an HP commercial printer.<sup>[102]</sup> For the cathode layer, an ink with PBSCF suspended in propylene glycol methyl ether and ethanol in 3:1 weight ratio was utilized. Additives, such as commercial dispersant DISPERBYK-2012, glycerol as a humectant and ethyl cellulose as a binder, were used to stabilize the ink and ensure printability. The formulated ink was ball-milled for 48 h at 120 rpm, while the Z number was determined to be 6.38, in the inkjet-printable region. The resulting PBSCF cathode printed onto the rest of the printed cell, was observed to be porous with no cracks or delamination issues occurring.

## 5. SOFC Advances with In Situ Inkjet Inks

To date, two methods for the inkjet printing of SOFC materials by in situ/precursor inks have been reported; the first exploits the nanodispersions of nucleated crystal phases and nanocrystals as obtained from synthetic routes such as the continuous hydrothermal flow synthesis (CHFS); while the second consists of using a mixture of metal precursor solutions or sol–gels as inks followed by the calcination of printed layers. Since, these inks are comprised of reactive chemicals, it is a common route to print in ambient cartridge temperature, to avoid further crystal growth and clogging of nozzles. Each of these two types of in situ inks will be presented separately, for each SOFC active material tested.

### 5.1. SOFCs from CHFS Inks

Continuous hydrothermal flow synthesis (CHFS or CHS) is a method used to synthesize nanostructures by using a high pressurized water flow, sometimes in supercritical conditions, mixed with an aqueous metal salt solution in an engineered mixer.<sup>[135]</sup> CHFS belongs in the greater category of the solvothermal synthesis techniques which is a batch-synthesis

process utilizing autoclaves, usually made of stainless steel, to synthesize crystalline materials by reaching high pressure conditions. However, the output of CHFS provides nanodispersed particles, which can be easily formulated into an inkjet-compatible water-based ink, by mixing in appropriate additives and/or solvents. As we already mentioned, the use of water as solvent in inkjet ink formulations presents many advantages in regards to availability, safety, cost, and green chemistry. Thus, utilizing CHFS nanodispersed products could offer further advantages like synthesis precision and scale-up, nanoparticles dispersion stability and synthesis-to-formulation automation. A schematic representation of a two-stage CHFS reactor is presented in Figure 10a.

In the last decades, solvothermal synthesis techniques have been employed in the synthesis of SOFC materials, from hydrothermal (in the case of solvent water), to microwave-assisted, and CHFS.<sup>[136–144]</sup> However, very limited research studies have been published on the utilization of CHFS to fabricate in situ inkjet inks, most likely due to the novelty involved. To the best

of our knowledge, no more than three such publications have been reported so far.<sup>[144–146]</sup> As a technical side note, it should be noted that these works constitute a hybrid between the ex situ and in situ ink development methods. This is the case since authors report on either isolating nanopowders or condensing the dispersions produced from CHFS, in order to use the as obtained wet powder or the produced dense slurry as a starting material to be redispersed in water.

Two such works have been published in 2019 by Rosa et al., reporting on the implementation of two separate continuous hydrothermal reactors.<sup>[145,146]</sup> One is a laboratory-scale two-step continuous hydrothermal reactor built at DTU Energy, which due to the two-step design offers an additional mixing stage for introduction of additional reactants or additives.<sup>[147]</sup> The second is a large-scale continuous hydrothermal reactor available by Promethean Particles Ltd., UK.<sup>[148]</sup>

In the case of the synthesis of YSZ nanodispersions, both reactors were tested.<sup>[145]</sup> For the synthesis with the DTU Energy reactor, precursors  $Zr(NO_3)_4$  and  $Y(NO_3)_3$  were mixed with

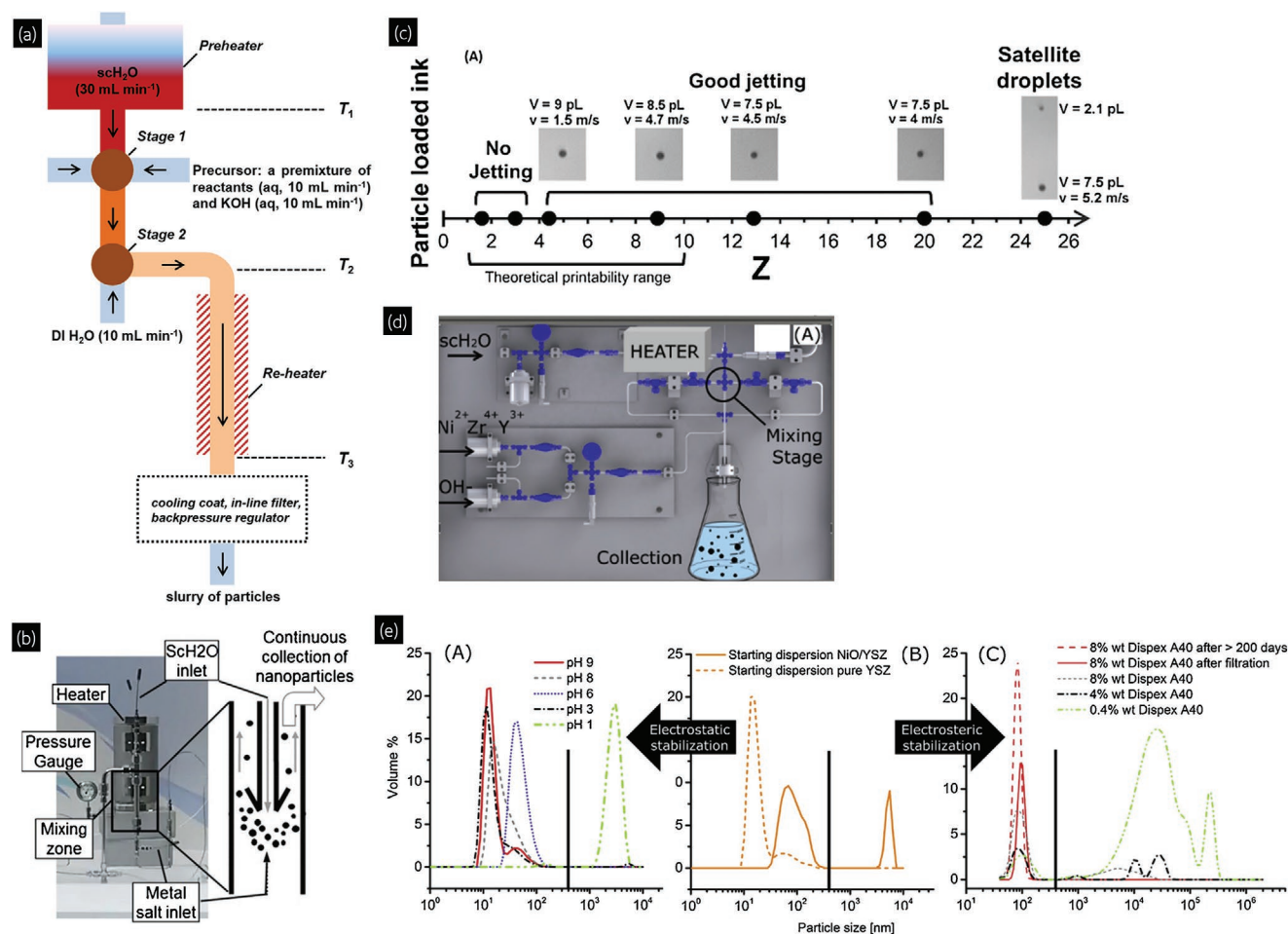


**Figure 10.** a) Schematic representation of the two-stage CHFS reactor; the flow rate of each DI  $H_2O$ /solutions stream is given in parentheses; arrows indicate the flow direction. Adapted with permission.<sup>[144]</sup> Copyright 2017, Wiley. b) Sketch of the CHFS reactor (Promethean Particles LTD.) with a magnified view of the mixing zone. Adapted with permission.<sup>[145]</sup> Copyright 2019, Elsevier. c) Jetting behavior of the formulated particle-loaded inks with different Z values. Adapted with permission.<sup>[145]</sup> Copyright 2019, Elsevier. d) Sketch of the continuous flow reactor. Adapted with permission.<sup>[146]</sup> Copyright 2019, Elsevier. e) Particle size distribution of the NiO-YSZ dispersion for the electrostatic- and electrosteric-stabilized inks. Adapted with permission.<sup>[146]</sup> Copyright 2019, Elsevier.

a stream of supercritical water at 397 °C and 270 bar, in 184 and 32 mmol L<sup>-1</sup> concentrations, respectively. After heating at 390 °C the slurry was cooled and collected. For the synthesis with the Promethean Particles Ltd. reactor (Figure 10b), the Zr(OH)<sub>2</sub>(C<sub>2</sub>H<sub>3</sub>O)<sub>2</sub> and Y(NO<sub>3</sub>)<sub>3</sub> precursors were mixed, at 20 mL min<sup>-1</sup> flow rate, with a stream of supercritical water at 375 °C and 241 bar. Tangential flow filtration was used to increase the final particle concentration. In both cases, the resulting nanodispersion was sonicated, then concentrated to a solid loading of 5.5 wt%. To formulate inkjet compatible inks PVP was added as a thickener, HCl for pH regulation and 2,4,7,9-Tetramethyl-5-decyne-4,7-diol ethoxylate at 2 wt% as a surfactant. By adding PVP thickener in various amounts the authors fabricated inks in a wide range of Z values, up to 25, to investigate their jettability. These YSZ inks were deposited onto presintered NiO–YSZ substrates, using a Pixdro LP50 inkjet printer equipped with a Dimatix printhead. Inks with Z values in the range of 4.4 to 20 demonstrated good jetting, as summarized in Figure 10c. Although such a jettable range in the Z number disagree with the literature (1 ≤ Z ≤ 10). The authors attributed this behavior to the small size (10 nm) and large surface area of their nanoparticles. The inkjet-printed layers were calcined at 800, 1000, and 1200 °C, with their porosity being reduced from 9 vol% in samples sintered at 800 °C, to 2 vol% at 1000 °C. In the case of samples calcined at 1200 °C, full densification of films was observed due to the extensive sintering of particles.

In the case of the NiO–YSZ nanodispersions synthesis, only the DTU Energy reactor was utilized (Figure 10d).<sup>[146]</sup> A precursor stream with a 8.3 mL min<sup>-1</sup> flow rate, consisting of ZrO(NO<sub>3</sub>)<sub>2</sub>, Y(NO<sub>3</sub>)<sub>3</sub>, and Ni(NO<sub>3</sub>)<sub>2</sub> in concentrations 31, 5.4, and 140 mmol L<sup>-1</sup>, respectively, was mixed at the first mixing stage with a stream of 1 mol L<sup>-1</sup> of KOH solution flowing at 9.8 mL min<sup>-1</sup>. This mixture was combined at the second mixing stage with a stream of supercritical water at 400 °C and 280 bar. After heating (385 °C) and centrifugation the obtained slurry was redispersed in water, in a multistep process, resulting in a dispersion with pH of ≈10–11.

One set of inks was prepared for electrostatic stabilization by mixing this slurry with isopropanol and propylene glycol and sonicating (final solid loading: 2.2 wt%). The optimal particle size distribution of a few hundred nanometers was observed at pH = 9. A second set of inks was formulated for electrosteric stabilization, by regulating the pH of the CHFS nanodispersion at 8.5 by HNO<sub>3</sub> addition along with varying amounts of dispersant Dispex A40 (final solid loading: 4.7 wt%). At a dispersant concentration of 8 wt% a narrow particle size distribution of a few dozen nanometers was obtained. The resulting particle size distributions for both inks are presented in Figure 10e, along with that of the starting CHFS nanodispersions.

Zeta values of the resulting inks were calculated to be 4.3 and 11.2, respectively. Even so, both inks appeared to be jettable, using the same Pixdro modified inkjet printer, as in the previous report. NiO–YSZ films deposited onto YSZ presintered substrates by multiple printing passes, were calcined using a multistep thermal procedure, with a maximum temperature of 1000 and 1295 °C for up to 6 h. SEM observation of layers calcined at 1000 °C revealed the presence of micrometer-sized agglomerates in films deposited with the first (isopropanol)

ink, while in films with the second (Dispex A40) ink were comprised of a uniform crack-free layer. Further study of the sintering of NiO–YSZ films printed by the second ink, at temperatures from 800 to 1295 °C was conducted. Above 1000 °C, shrinkage of films was noted from about 500 to 300 nm, while above 1295 °C YSZ diffusion and Ni aggregation was presented on the surface.

The third CHFS study used the same two step reactor to synthesize GDC powders which were then isolated as a wet product.<sup>[144]</sup> Nitrate precursor solutions, of 40 mmol L<sup>-1</sup> concentrations of metal cation, and KOH solutions of various concentrations, were dissolved in a 30 mL min<sup>-1</sup> heated water flow at 369 °C. This mixture was added at the second mixing stage, to a distilled water flow of 10 mL min<sup>-1</sup> at room temperature, with the pressure being kept at 26 MPa. The resulting GDC nanodispersion was collected and nanoparticles were isolated by centrifugation. The wet GDC nanopowders were then redispersed in water to form two distinct suspension inks, one to print onto NiO–GDC and another for NiO–YSZ substrates.

For the first substrates, a Ceradrop X-Serie piezoelectric inkjet printer equipped with a Dimatix printhead was used, whereas a Pixdro LP50 inkjet printer, again equipped with a Dimatix printhead, was used for the second. The first ink was fabricated by dispersing the wet GDC powders in water in the presence of Dispex A40 with the use of an ultrasonic processor. Then 10 mg cm<sup>-3</sup> of PEG-35000 and 0.2 mg cm<sup>-3</sup> Natsurf 265 were added to adjust viscosity and surface tension. For the second ink PEG was not added, but only Natsurf 265 at 6 mg cm<sup>-3</sup>. Printed layers were thermally sintered at 1300 °C and their morphology was observed with a microscope. In the case of the ink printed onto NiO–GDC, the authors reported cracks in the films upon sintering of more than five layers. Conversely, the single- and five-layer films were not adequately dense or consistent. In the case of the ink printed onto presintered NiO–YSZ, again even after ten printing passes no continuous film was accomplished, with formation of GDC “islands” probably due to the shrinkage of the layer after the sintering step.

## 5.2. SOFCs from Precursor Solution/Sol–Gel Inks

The basis of precursor in situ ink development lies on utilizing mixed precursor solutions of metals for IJP, followed by the calcination of the printed layers, which will result in a continuous film of the in situ synthesized active materials. In this method, precursor solutions of metals should be synthetically tested by tuning their relative concentration, so to reach the desired atomic ratio in the final product. Most published works rely on aqueous solutions of metal nitrates. However, the use of acetate or propoxide precursors have been reported, as well as synthetic procedures with water–organic solutions, organic additives, or/and organic solvents.

One of the most facile procedures was reported in 2013 by Da’as et al. in a conference proceeding.<sup>[149]</sup> By dissolving precursors La(NO<sub>3</sub>)<sub>3</sub>·6H<sub>2</sub>O, Sr(NO<sub>3</sub>)<sub>2</sub>, and Mn(NO<sub>3</sub>)<sub>2</sub>·4H<sub>2</sub>O in deionized water an in situ printable LSM ink was formulated and coated on porous YSZ substrates by inkjet impregnation, using a FujiFilm Dimatix DMP 2800 inkjet printer. Optimized

printing parameters in this work include the drop spacing, the substrate temperature, the cartridge height and the number of printing passes. All printed layers were dried at 100 °C, followed by a calcination at 800 °C for 2 h. Resulting cathodes displayed a brown color after drying, indicating decomposition of the nitrate salts, followed by a typical black color after calcination.

In a more recent publication, Venezia et al. reported on the infiltration of the cathode layer of a commercial SOFC cell consisting of LSCF|YSZ|NiO–GDC (CEREL, Poland) with developed LSC and GDC precursor inks.<sup>[150]</sup> To formulate the GDC ink, stoichiometric amounts of  $\text{Ce}(\text{NO}_3)_3 \cdot 6\text{H}_2\text{O}$  and  $\text{Gd}(\text{NO}_3)_3 \cdot 6\text{H}_2\text{O}$  were dissolved in ethanol by stirring at 40 °C, with urea as a complexing agent. The metals to urea molar ratio was 1:1.5, while the total metal ion concentration was 0.75 M. For the LSC ink the same procedure was followed with the appropriate nitrate precursors. Inkjet infiltration of the cathodes of the commercial cells was performed with a custom microvalve nozzle Domino Macrojet inkjet printer. Three printing passes were required for the “single-step” infiltration of maximum loading of the cathode layers with either of the inks. Resulting samples were calcined at 700 °C and observed with a microscope after sintering and after 72 h of electrochemical testing via electrochemical impedance spectroscopy (EIS) under  $\text{H}_2$  and  $\text{O}_2$  atmospheres, at the anode and cathode respectively, at open-circuit voltage (OCV) in 0.1 Hz–100 kHz frequency range. Before testing, images of the infiltrated cells displayed a uniform coverage of the cathode layers with fine nanoparticles. However, after 72 h of aging and EIS testing at 700 °C, both infiltrated materials seem to aggregate into larger nanoparticles, forming chains and flocculent structures, most probably due to strontium surface separation.

As mentioned in the previous section on “ex situ inks,” in their 2017 publication Tomov et al. reported on the infiltration with GDC in situ inks of a previously inkjet-printed LSCF–GDC cathode layer.<sup>[130]</sup> The precursor/in situ GDC ink was formulated by dissolving citric acid,  $\text{Ce}(\text{NO}_3)_3 \cdot 6\text{H}_2\text{O}$  and  $\text{Gd}(\text{NO}_3)_3 \cdot 6\text{H}_2\text{O}$  in solvent ethanol, with a molar ratio of 1:1.5 between metal ions and citric acid. Infiltration of the symmetrical cathode layers, printed previously on both sides of dense GDC pellets, was performed by printing multiple passes of the GDC ink, with intermediate drying after each printing pass at temperatures from 20 to 120 °C. Infiltrated cells were calcined at 700 °C for 1 h, and infiltrated GDC loading was calculated at a 4:100 weight ratio in regards to the previously printed composite cathode layer. Through SEM, the infiltrated GDC was observed to consist of nanoparticles varying in size between 10 and 20 nm, uniformly presented throughout the cathode surface.

Same authors, published as Mitchell-Williams et al., achieved the infiltration of GDC into the anode layer of a commercially available NiO–YSZ|YSZ|LSCF cell (CEREL, Poland).<sup>[151]</sup> For the ink formulation, stoichiometric amounts of  $\text{Ce}(\text{NO}_3)_3 \cdot 6\text{H}_2\text{O}$  and  $\text{Gd}(\text{NO}_3)_3 \cdot 6\text{H}_2\text{O}$  were dissolved in either water or propionic acid (PPA). In order to regulate the surface tension of the water-based ink, 3 wt% of surfactant Triton X-100 was added, relative to the nitrate concentration. The total metal ion concentration of each ink was calculated to be 1.0 M for the water-based and 0.5 M for the PPA-based.

Printing was performed by the same custom Domino Macrojet printer. For the PPA-based inks four printed passes were required, while for the water-based only two, to reach the maximum possible metal-ion concentration to be absorbed by the porous anode. To achieve greater GDC loadings, infiltrated cells were thermally treated at 500 °C and this printing step was repeated, doubling the printing passes for each ink. The resulting cells were then calcined at 800 °C for half an hour, resulting in a final 1 wt% mass loading of GDC in regards to the total original weight of the cell. Although the two inks behaved differently regarding their rheological and wetting properties, with the PPA-based ink displaying better wetting than the water-based (Figure 11a), the SEM observation of the infiltrated surfaces revealed similar results. In both samples GDC nanoparticles displayed an approximate mean size of  $56 \pm 16$  nm and were evenly distributed throughout the anode layer.

On a similar note, in their 2020 publication, Kim et al. printed a precursor ink of LSC onto a previously inkjet-printed LSCF cathode layer, in order to infiltrate the cathode backbone layer with a surface catalyst to enhance cathode performance (Figure 11b).<sup>[152]</sup> The infiltration ink was developed by mixing precursors  $\text{La}(\text{NO}_3)_3 \cdot 6\text{H}_2\text{O}$ ,  $\text{Sr}(\text{NO}_3)_2$ , and  $\text{Co}(\text{NO}_3)_2 \cdot 6\text{H}_2\text{O}$  in a 0.6:0.4:1 molar ratio, in a mixture of water and ethanol in 56 and 44 wt% concentrations, respectively. The resulting solution (0.05 M) was mixed with glycine used as chelating agent and PVP as a surfactant at a concentration of 10.6 and 1.68 mg mL<sup>-1</sup>, respectively. Infiltration was carried out using a commercial inkjet printer (HP 1110), while the printing passes varied between 5, 10, and 20 cycles. The final printed layers were calcined at 550 °C for 1 h, and then their morphology was observed via SEM, as presented in Figure 11c for the bare LSCF cathode and Figure 11d for the LSC-infiltrated (10 printing passes). Infiltrated LSC particles of  $\approx 5$ –10 nm were observed to be uniformly distributed onto the LSCF cathode backbone, with the exception of the five printed passes layer where infiltration was less uniform.

In an earlier publication by Wang et al., the inkjet printing of in situ sol–gel GDC ink formulated by the use of acetate precursors, was reported.<sup>[153]</sup> More specifically, precursors  $\text{Ce}(\text{CH}_3\text{CO}_2)_3 \cdot x\text{H}_2\text{O}$  and  $\text{Gd}(\text{CH}_3\text{CO}_2)_3 \cdot x\text{H}_2\text{O}$  were dissolved in PPA under reflux at 120 °C over 4 h. After filtration of the solution, the precursor ink was diluted by 1-propanol addition, doubling its volume, in order to regulate viscosity of the ink, thus reaching a final total metal ion concentration of 0.75 M. The GDC electrolyte layer was deposited onto presintered NiO–YSZ substrates (CEREL, Poland) by ten printing passes at 100 °C substrate temperature. Between each pass at 400 °C an intermediate thermal treatment was performed, in order to remove the majority of organic residues, while the final printed GDC layer was thermally treated at 650 °C. Finally, samples were calcined at three distinct temperatures 900, 1000, and 1100 °C for 1 h, in order to explore the temperature effect on sintering. By SEM observation, differential scanning calorimetry (DSC) measurements of precursor inks and computed DSC analysis, the authors concluded that the sintering stage manifests at 1100 °C, with grains merging their boundaries to form a dense layer. Since the electrolyte layer of an SOFC needs to be dense, this temperature was selected as the optimal for postprinting sintering. The thermally treated and sintered GDC

films, deposited by ten printing passes, displayed a porosity of 5%. In order to reduce it further, the authors repeated the printing and thermal processes, up to a total of 20 printing passes, achieving a decreased porosity of 2%.

In a recent publication, Rahumi et al. used a single-step wet-chemical synthesis of NiO–SDC as an in situ ink for IJP of anode layers in a symmetrical half-cell.<sup>[154]</sup> The NiO–SDC ink was formulated by dissolving nitrate hexahydrates of Ni(II), Ce(III), and Sm(III) in deionized water, at a total concentration of precursors of 0.3 M. Additives Triton X-100 (1.5 vol%) and a 0.2 M solution of (NH<sub>4</sub>)<sub>2</sub>CO<sub>3</sub> (0.75 vol%) were added as a surfactant and a precipitant, respectively, and then mixed vigorously for seven days in room temperature. The final ink displayed impressive dispersion stability, with a mean-diameter of 11.85 nm for the as-prepared ink and 10.03 nm after 6 months of storage, with no visible phase separation. The Z value of the ink was calculated to be 796, within the jettable range. Symmetrical anodes were fabricated, using an Epson Corp. L805 inkjet printer, on each side of a commercial ScCeSZ dense electrolyte (Fuel Cell, USA) by printing 50 passes on each. Afterward, a multistep sintering at up to 1250 °C for 2 h (1 °C min<sup>-1</sup>) was conducted. The crystal structure of the synthesized NiO–SDC film was confirmed by XRD, while SEM observations revealed a smooth porous surface, with a thickness ≈15–25 μm, consisting of nanoparticles of 60 nm in average size. The final cell efficiency was studied and compared to an

identical cell (Ni–SDC|ScCeSZ|Ni–SDC) fabricated by screen-printing (see Section 6).

In 2017, Gadea et al. reported on the in situ printing of YSZ thin films onto different substrates; commercial quartz, commercial polycrystalline alumina, and fabricated NiO–YSZ.<sup>[155]</sup> In this study a commercial propoxide precursor Zr(OPr)<sub>4</sub>, dispersed in propanol at 70 wt%, was mixed with nucleophilic agent and ligand *N*-methyl-diethanolamine (MDEA) in ethanol, along with an aqueous solution of dopant Y(NO<sub>3</sub>)<sub>3</sub>·6H<sub>2</sub>O. Four distinct synthetic parameters were tested, i.e., the zirconium concentration in the precursor ink, the MDEA to Zr(OPr)<sub>4</sub> molar ratio (also referred to as complexation ratio), the water to ethanol volume ratio and the aging time. The inks were studied by observing the dispersion stability, measuring their viscosity and surface tension, and calculating their Z value. A graphical presentation of the inks jettability is presented in Figure 11e, where the Z number of inks is plotted in regards to the MDEA/Zr(OPr)<sub>4</sub> complexation ratio for different zirconium concentrations and aging times, where the green area constitutes the jettable region 1 ≤ Z < 3 for inks tested.

Results indicated that lower concentrations of zirconium achieved better dispersion stability during storage, thus a concentration of 0.1 g mL<sup>-1</sup> was chosen. Additionally, increasing the MDEA to Zr(OPr)<sub>4</sub> molar ratio improved the stability and printability over time, with an optimal value of 12:1. Regarding the water to ethanol volume ratio, all inks prepared with the

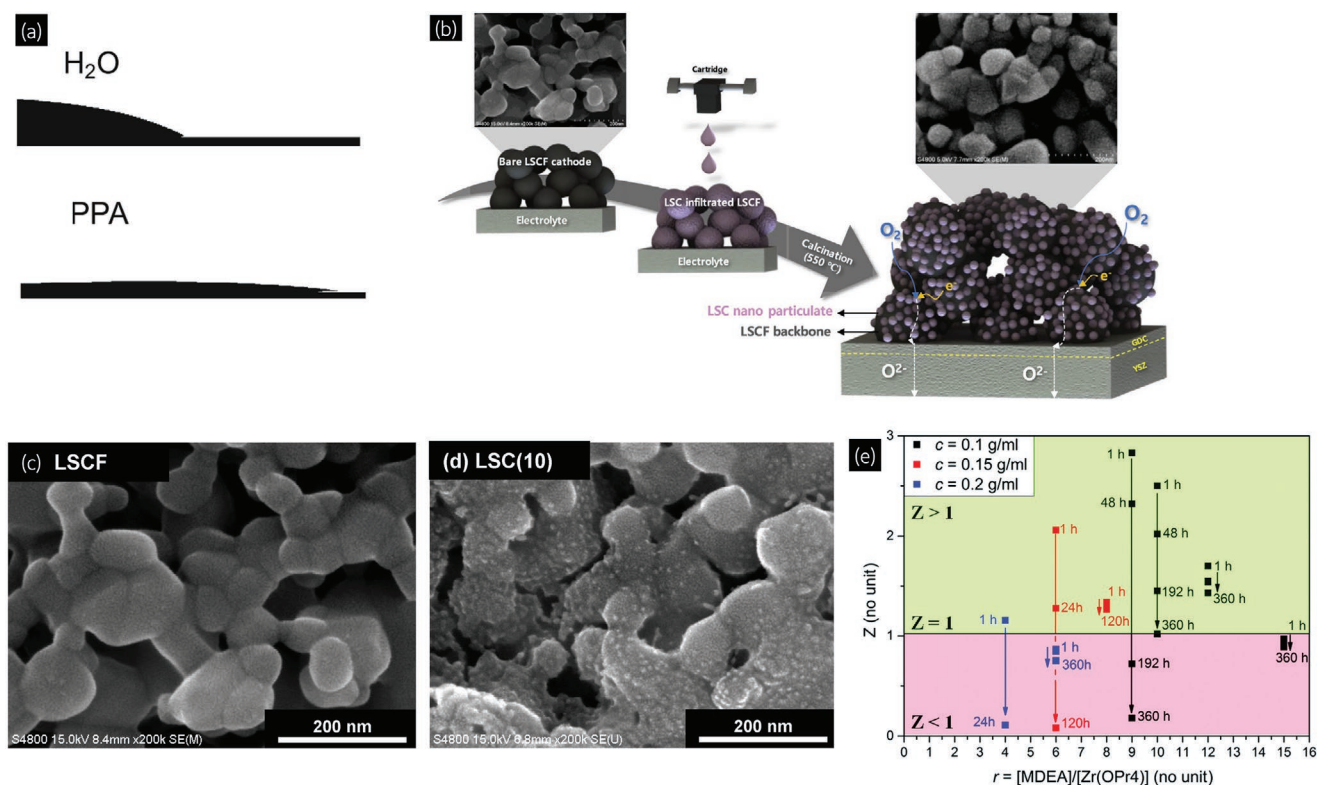


**Figure 11.** a) Contact angle observations on polycrystalline, dense YSZ substrate illustrating the difference in wetting between the water-based and the PPA-based inks. Adapted with permission.<sup>[151]</sup> Copyright 2017, Springer. b) Schematic of IJP process for the infiltration of LSC particles on the surface of LSCF cathode, with highlighted SEM images of LSCF cathode c) before and d) after LSC-infiltration, as obtained after ten printing passes and calcination at 550 °C. Adapted with permission.<sup>[152]</sup> Copyright 2020, Elsevier. e) Ink jettability at different concentrations and aging time versus complexation ratio. Adapted with permission.<sup>[155]</sup> Copyright 2017, RSC.

mentioned optimal parameters were equally printable and stable over time. However, in order to choose an optimum solvent ratio, other ink properties were considered, such as droplet formation, wettability, drying speed, and nozzle clogging, resulting a 60:40 optimal water to ethanol volume ratio. The Z value of the optimal sol–gel ink was calculated to be 1.64, in the inkjet-printable region. After printing, YSZ layers were calcined at 500 °C and observed to display different shrinkage and cracking depending on the substrate used. The most promising results were achieved on the more flat and rigid substrates, most probably due to their lower porosity, with an average single printing pass thickness of 150 nm regardless of the substrate used.

In a recent publication, Perin et al. adopted a hybrid route of ink development, by combining their previous reports to formulate a composite GDC–YSZ ink by mixing CHFS ink of GDC powders with a precursor ink of YSZ.<sup>[156]</sup> The CHFS water-based GDC ink was based on the publication by Xu et al.,<sup>[144]</sup> while the sol–gel precursor YSZ ink was based on the publication by Gadea et al.<sup>[155]</sup> In more detail, GDC powders, synthesized by CHFS, were dispersed in water at 7.1 wt% solid loading by addition of dispersant Dispex A40 and treated in an ultrasonic processor. On the other hand, the YSZ precursor ink was formulated by adding ligand MDEA to commercial Zr(OPr)<sub>4</sub>, dispersed in 1-propanol at 70 wt%, with an optimized molar ratio of 12:1, along with an unspecified yttrium precursor for doping. Molar ratio between GDC and YSZ in the final composite ink was tuned at 1:3.3, and the ink was filtered before printing onto a sapphire substrate with a Pixdro LP50 inkjet printer equipped with a Dimatix printhead. In order to establish the temperature required for the thermal annealing process, thermal XRD characterization of inkjet-printed layers was conducted. The analysis revealed YSZ peaks after 400 °C, while above 800 and 900 °C peaks from GDC nanoparticles decrease in intensity, which the authors attributed to the diffusion of gadolinium and cerium cations at higher temperatures. Thus, printed layers were calcined at 750 °C for 6 h and observed by SEM, revealing a continuous YSZ matrix of 10 nm grains, with embedded GDC aggregates in the form of sub-micrometer clusters.

Finally, the publication of Shimada et al. reported on the impregnation by IJP of yttrium-doped barium zirconate (BZY) onto Ni–YSZ anodes, utilizing an inkjet apparatus by Cluster Technology, with a PIJ-40NSET print-head and nozzles of ≈40 μm in diameter.<sup>[157]</sup> By using a spray pyrolysis synthesized NiO–YSZ powders, they painted the one side of the commercial ScCeSZ (Japan Fine Ceramics) electrolyte. The in situ ink for BZY-infiltration on the painted anodes was formulated by dissolving chlorides of yttrium, zirconium and barium at a concentration of 0.5 mol L<sup>-1</sup>. After IJP deposition, the infiltrated samples were sintered in air at 1300 °C for 4 h. From the SEM pictures it was observed that by increasing the amount of infiltrated BZY the morphology of the anodes is modified, presenting a decreased porosity. By changing the amount of BZY infiltration, an optimal NiO:YSZ:BZY weight ratio of 60:40:3 was reported, which enabled a sufficiently high porosity with adequate material incorporated in the anode film.

## 6. Inkjet-Printed SOFC Performance

The majority of published works on inkjet-printed SOFC components are focused on ink development, the inkjet printing process and the obtained quality of the deposited layers on the employed substrates. Unfortunately, so far very few studies have reported on the achieved electrochemical performance of inkjet-printed SOFCs. This fact alone highlights the early stage of implementation of IJP techniques on SOFC fabrication and thus the novelty of this topic. However, some of the works discussed in this review, with at least one inkjet-printed layer, report on SOFC performance and their results are summarized in Table 1.

### 6.1. SOFC Performance with Inkjet-Printed Electrolytes

Among its other advantages, inkjet printing can deposit layers of sub-micrometer thickness and facilitate the fabrication of very thin, yet dense, electrolytes. This is extremely desirable in SOFC performance since thinner electrolytes are associated with lower ohmic resistances and consequently higher current and power densities are achievable. In fact, among the works of Table 1, both the highest and second highest peak power density (PPD) are reported for cells with inkjet-printed YSZ electrolytes, with 1.5 W cm<sup>-2</sup> at 800 °C and 1.04 W cm<sup>-2</sup> at 750 °C.

The earliest report on the performance of an SOFC with inkjet-printed components was by Young et al. in 2008.<sup>[111]</sup> The authors printed a NiO–YSZ interlayer and a YSZ electrolyte layer (both ≈6 μm thick) on a commercial anode support of NiO–YSZ and, in combination with a hand painted LSM–YSZ cathode. They reported a PPD of 175 mW cm<sup>-2</sup> at 750 °C using dry H<sub>2</sub> as the fuel, while the OCV was ≈1.04 V. The corresponding electrochemical impedance spectra (EIS) at open circuit showed an overall area specific resistance (ASR) of ≈3.75 Ohm cm<sup>2</sup>, with an ohmic contribution (the main effect of electrolyte thickness) of 0.38 Ohm cm<sup>2</sup>, i.e., one tenth of the overall resistance. However, the cell was not very stable at higher temperatures.

The following year, the same group expanded their printing methods by inkjet printing not only the anode interlayer and electrolyte, but also an LSM–YSZ cathode and an LSM current collector.<sup>[110,112]</sup> This time the electrolyte layer was rather thicker, at 16 μm, while the interlayer thickness varied between 4 and 10 μm, and the cathode film was between 40 and 50 μm. In this work, the cells were more stable at 800 and even 850 °C, where PPDs of 210 and 460 W cm<sup>-2</sup>, respectively, were achieved when employing the same fuel. The OCVs were also slightly higher (1.1–1.13 V) than with their previous cell, implying better gas tightness, a possible effect of the thicker electrolyte. The overall and ohmic ASRs were 1 and 0.2 Ohm cm<sup>2</sup>, respectively, at 850 °C, while the corresponding values at 750 °C were 3.75 and 0.4 Ω cm<sup>2</sup>. These slightly higher values, compared to their previous cell, could be attributed to the increase in the thickness of the electrolyte layer.

In 2010, Tomov et al. reported on the performance of an inkjet-printed YSZ electrolyte, deposited on a square NiO–YSZ support, which would function as the anode.<sup>[121]</sup> After ten printing passes with a 5 wt% YSZ ink, they obtained dense

**Table 1.** Performance data for SOFCs with at least one inkjet-printed component layer (interl = interlayer film; OCV = open-circuit voltage; PPD = peak power density; SI = suspension ink; PI = precursor ink; WB = water based; OB = organic based; EW = ethanol–water solvent. (A more detailed version of Table S1 is presented as the Supporting Information spread sheet)).

Inkjet-printed layer	SOFC	Electrolyte thickness [ $\mu\text{m}$ ]	OCV [V]	PPD [ $\text{mW}\cdot\text{cm}^{-2}$ ]	Temperature [ $^{\circ}\text{C}$ ]	Anode feed/fuel	Ink/solvent type	Reference
NiO–YSZ (interl) YSZ	NiO–YSZ NiO–YSZ (interl) YSZ LSM–YSZ	6	0.99 – 1.13	175	750	Dry H <sub>2</sub>	SI/OB	[111]
NiO–YSZ (interl) YSZ LSM–YSZ LSM	NiO–YSZ NiO–YSZ (interl) YSZ LSM–YSZ LSM	16	1.13	210	800	Dry H <sub>2</sub>	SI/OB	[112]
NiO–YSZ (interl) YSZ LSM–YSZ LSM	NiO–YSZ NiO–YSZ (interl) YSZ LSM–YSZ LSM	16	1.1	460	850	Dry H <sub>2</sub>	SI/OB	[110]
YSZ	NiO–YSZ YSZ LSM–YSZ LSM	$\approx 5.7$	1.01	170	800	(5%) Humidified H <sub>2</sub>	SI/OB	[121]
LSCF–GDC	NiO–GDC GDC LSCF–GDC LSCF–GDC	50	0.94	710	600	H <sub>2</sub> in N <sub>2</sub> (4% H <sub>2</sub> O)	SI/WB	[99]
YSZ	NiO–YSZ YSZ LSM–YSZ LSM	Less than 6	1.01	170	800	(5%) Humidified H <sub>2</sub>	SI/OB	[123]
NiO–CuO–YSZ	NiO–CuO–YSZ YSZ   LSM–GDC LSM	200	–	96	800	CO <sub>2</sub> and carbon fuel	SI + PI/OB	[124]
NiO–YSZ or NiO–GDC	NiO–GDC YSZ LSM–GDC LSM	200	1.05	80	780	Ar and carbon fuel	SI + PI/OB	[126]
YSZ SDC (interl)	NiO–YSZ YSZ   SDC BSCF	7.5 YSZ and 2 SDC	1.1	1040	750	H <sub>2</sub>	SI/-	[104]
SSC–SDC	NiO–YSZ YSZ SDC SSC–SDC	–	1.1	950	750	H <sub>2</sub>	SI/WB	[105]
YSZ	NiO–YSZ NiO–YSZ YSZ LSM–YSZ	1.2	1.07	1500	800	(4%) Humidified H <sub>2</sub>	SI/WB	[103]
YSZ	NiO–YSZ YSZ LSM–GDC	$\approx 5.7$	1.077	220	800	Humidified H <sub>2</sub> in N <sub>2</sub>	SI + PI/OB	[128]
YSZ	NiO–YSZ YSZ LSM–YSZ LSM	23	0.84	–	718	9:1 CO <sub>2</sub> :CO	SI/WB	[106]
LSCF	NiO–YSZ NiO–YSZ YSZ GDC LSCF	10	1.14	377	600	Humidified H <sub>2</sub>	SI/WB	[100]
LSCF or LSCF–GDC GDC buffer	NiO–YSZ NiO–YSZ YSZ GDC LSCF–GDC	10	1.15	574	650	Humidified H <sub>2</sub>	SI/EW	[101]
NiO–GDC and infiltration GDC	NiO–YSZ NiO–GDC: GDC LSCF–GDC LSCF	5	0.9	380	600	Humidified H <sub>2</sub>	SI + PI/OB	[129]
YSZ	NiO–YSZ NiO–YSZ symmetric cell	0.15	–	–	750	Synthetic air	PI/WB	[155]
infiltration GDC	GDC:NiO–YSZ YSZ LSCF–GDC	–	0.98	$\approx 75$	800	( $\approx 4\%$ ) Humidified H <sub>2</sub>	PI/OB	[151]
LSCF–GDC and infiltration GDC	LSCF–GDC GDC LSCF–GDC:GDC	600	–	–	550	Ambient air	SI + PI/OB	[130]
YSZ and LSM–YSZ	Ni–YSZ YSZ YSZ–LSM LSM	$\approx 10$	–	690	788	Dry H <sub>2</sub>	SI/WB + OB	[107]
GDC–YSZ	Ag GDC–YSZ Ag	–	–	–	600	Air	SI/-	[156]
infil LSC or infil GDC	NiO–GDC 3YSZ LSCF:LSC	–	1.04	350	700	Humidified H <sub>2</sub>	PI/OB	[150]
NiO–YSZ (interl) YSZ GDC (interl) PBSCF	NiO–YSZ NiO–YSZ YSZ GDC PBSCF	0.8 YSZ and 0.5 GDC	1.14	730	650	Humidified H <sub>2</sub>	SI/EW + OB	[102]
Ag–SDC	Ag–SDC SDC Pt	3	1.05	56	450	H <sub>2</sub>	SI/OB	[134]
NiO–SDC	NiO–SDC Sc–CeZrO <sub>2</sub>  NiO–SDC	15	–	–	800	H <sub>2</sub>	PI/WB	[154]
Infiltration BZY	(BZY) NiO–YSZ Sc–CeZrO <sub>2</sub>  YSZ–LSM	–	1.16	790	900	(3%) Humidified H <sub>2</sub>	PI/WB	[157]

YSZ layers with less than 6  $\mu\text{m}$  thick, after sintering, on top of which they screen printed successive LSM–YSZ and LSM layers to act as the cathode. In this cell, with humidified hydrogen (5% H<sub>2</sub>O) flowing over anode and static air over the cathode, they achieved an OCV of 1.01 V and a PPD of 170  $\text{mW cm}^{-2}$  at 800  $^{\circ}\text{C}$ , while their impedance spectra indicated overall and

ohmic ASRs of 11.25 and 1.63  $\Omega \text{ cm}^2$ , respectively. The latter two values imply that the electrolyte contribution to the overall cell resistance was minimal, pointing to the need for improvements in the electrodes, or airflow over the cathode. When they retested such electrolytes in 2016 with simple LSM cathodes the achieved PPD increased to 220  $\text{mW cm}^{-2}$ .<sup>[128]</sup>

In 2013, two other publications reported SOFC performances with inkjet-printed YSZ electrolytes. The first involved several European groups, who used  $\alpha$ -terpineol as the solvent and commercial YSZ powders to obtain dense sintered layers of  $\approx 6 \mu\text{m}$ .<sup>[123]</sup> Conventional methods were used to deposit LSM–YSZ and LSM layers to create single cells, which were tested at 700–800 °C. Using 5% H<sub>2</sub>O in H<sub>2</sub> as their anode feed and ambient air over the cathode they achieved an OCV of 1.01 V and a PPD of 170 mW cm<sup>-2</sup> at 800 °C. The second publication, from a Sino-Australian cooperation, involved water-based inks for the printing of both a dense YSZ electrolyte (7.5  $\mu\text{m}$ ) and an SDC buffer layer (2  $\mu\text{m}$ ) topped with a Ba<sub>0.5</sub>Sr<sub>0.5</sub>Co<sub>0.8</sub>Fe<sub>0.2</sub>O<sub>3- $\delta$</sub>  (BSCF) cathode deposited by wet powder spraying.<sup>[104]</sup> The authors reported an OCV of 1.1 V and a PPD of 1040 mW cm<sup>-2</sup> at 750 °C, with dry H<sub>2</sub> as fuel and ambient air over the cathode. Their impedance spectra revealed a total ASR of 0.9  $\Omega \text{ cm}^2$  and an ohmic contribution of 0.25  $\Omega \text{ cm}^2$ .

The highest PPD achieved so far with inkjet-printed SOFCs, was reported by Esposito et al. in 2015.<sup>[103]</sup> This group used nanometric YSZ powder in an aqueous suspension to prepare a 4 × 4 cm electrolyte of only 1.2  $\mu\text{m}$  thickness supported on Ni–YSZ substrate. With a screen printed LSM–YSZ/LSM cathode, H<sub>2</sub> flowing over the anode and air on the cathode they produced 1.5 W cm<sup>-2</sup> at 800 °C, starting from an OCV of 1.08 V. Aside from reporting the highest PPD, this publication records one of the lowest SOFC electrolyte thicknesses, as presented in Table 1.

The same year Gadea et al. prepared in situ inks using yttrium nitrate and zirconium propoxide and a modified HP Deskjet 1010 printer.<sup>[155]</sup> They reported the fabrication of thin (125 nm), dense, nanocrystalline YSZ films after a single calcination/sintering step at 500 °C. In spite of this achievement, they did not use these films in an SOFC configuration, but measured only the lateral impedance of the film with two silver electrodes painted about 1 mm apart. The resulting conductivities (in Arrhenius plot) were found to be close to the lowest typically reported values for thin YSZ films. The next year, they reported on the use of a hybrid ink consisting of GDC powder and YSZ precursors.<sup>[156]</sup> The conductivity plots of the resulting thin films lay between the literature plots for single crystal YSZ and single crystal GDC and with lower activation energy.

In 2016, Farandos et al. prepared dense, inkjet-printed YSZ electrolytes (23  $\mu\text{m}$ ) on tape cast NiO–YSZ supports using aqueous, colloidal, water-based inks.<sup>[106]</sup> Besides the electrolyte layers (12 passes) they also experimented in printing various 3D structures, involving several dozen printing passes. To complete their cells, they brush-painted LSM–YSZ cathodes on the co-sintered anode–electrolyte bilayers. They used these cells as CO<sub>2</sub> electrolyzers, obtaining ASRs of 0.2 and 0.66  $\Omega \text{ cm}^2$ , for the ohmic and electrode polarization (overall ASR minus ohmic ASR) contributions, respectively. Two years later, they reduced the electrolyte thickness to about 9  $\mu\text{m}$  and also printed the LSM–YSZ cathode ( $\approx 20 \mu\text{m}$ ), with a hand painted LSM current collector completing the cell.<sup>[107]</sup> Using dry H<sub>2</sub> as their fuel and static air over the cathode, they obtained a PPD of 690 mW cm<sup>-2</sup> at 788 °C, but unfortunately reported no cell voltage data. Their Nyquist plots showed an overall ASR of 0.47  $\Omega \text{ cm}^2$  with the ohmic component below 0.1  $\Omega \text{ cm}^2$ . This drop in the ohmic

value is expected with this decrease in electrolyte thickness (from 23 to 9  $\mu\text{m}$ ).

Although most printing efforts employed YSZ electrolytes there is one study wherein a GDC electrolyte was inkjet-printed and the fuel cell performance is reported.<sup>[129]</sup> After printing a NiO–GDC interlayer and infiltrating some GDC into the resulting bilayer, the authors used a different GDC suspension ink to produce a GDC electrolyte layer (5  $\mu\text{m}$  after sintering). Using an LSCF-based cathode and humidified H<sub>2</sub> as the fuel, they achieved an OCV of 0.9 V and a PPD of just under 0.4 W cm<sup>-2</sup> at 600 °C, while reporting an ASR of 0.136  $\Omega \text{ cm}^2$ . This PPD was about 2.5 times higher than that obtained with a noninfiltrated anode (0.15 W cm<sup>-2</sup>).

## 6.2. SOFC Performance with Inkjet-Printed Electrodes

There are several studies reporting performance with inkjet-printed electrodes, either on similarly printed or on conventional electrolytes. Most of these focus on the printing of cathodic electrodes, while the printing of anodic layers is usually limited to a thin interlayer between the NiO–YSZ support and the electrolyte layer.<sup>[102,110–112]</sup>

Two publications in 2013 do, in fact, report on the performance of fully inkjet-printed anodes in direct carbon SOFCs (DC-SOFCs).<sup>[124,126]</sup> In both works commercial YSZ electrolyte disks (200  $\mu\text{m}$  thickness) and screen printed LSM–GDC/LSM cathodes were used, with carbon as the fuel, produced from the radio frequency plasma splitting of methane. In one of these publications, the authors examined the effect of Cu inkjet infiltration on the performance of the inkjet-printed Ni–YSZ anode and found that, at 800 and 850 °C with Ar feed to the fuel compartment (anode), their PPD was about 30% higher in the case of Cu infiltration.<sup>[124]</sup> They also found that screen printed Ni–YSZ anodes (50  $\mu\text{m}$ ) gave about the same performance as their inkjet-printed counterparts (30  $\mu\text{m}$ ) at temperatures above 750 °C, with the same anode feeds. Finally, when they switched the anode feed to CO<sub>2</sub> (which reacts with the solid carbon according to the Boudouard reaction, as opposed to the inert Ar) the Cu-infiltrated inkjet-printed anodes were about 20% better than the non-infiltrated inkjet-printed ones. In the second publication, by largely the same authors, the replacement of YSZ with GDC in the anode was examined.<sup>[126]</sup> Their results showed that, with Ar feed and the same solid fuel, the Ni–GDC anodes achieved twice as high PPDs as the Ni–YSZ ones at 750–780 °C.

The first reports on inkjet-printed cathodes appeared in 2009, when Sureshini et al. expanded their work from previous years (printing of the electrolyte) to the printing of an LSM–YSZ/LSM cathode bilayer.<sup>[110,112]</sup> After optimizing the printing parameters they obtained bilayers of 40–50  $\mu\text{m}$  thickness. When compared with the performance of hand-pasted cathodes the PPDs at 800 and 850 °C were about the same in dry hydrogen (about 320 and 460 mW cm<sup>-2</sup> vs 320 and 450 mW cm<sup>-2</sup>), but the inkjet-printed cathodes performed better as the temperature tended toward 600 °C with dry H<sub>2</sub> fed to the anode.<sup>[112]</sup> This is likely due to the more precise control of the layer thickness with inkjet printing, indicating the potential of this method for IT- and LT-SOFC fabrication.

The following year, Yashiro et al. tested LSCF–GDC composite cathodes deposited by various methods on a GDC electrolyte, itself supported on a NiO–GDC anode support.<sup>[99]</sup> They compared an inkjet-printed cathode with a painted one and with a double-layer composed of a painted layer on top of a printed one. The best performance, using humidified H<sub>2</sub>/N<sub>2</sub> anode feed, was achieved with the double-layer cathode (OCV: 0.94 V, PPD: 710 mW cm<sup>-2</sup> at 600 °C) which, interestingly, was the thickest of the three. On the other hand, the thickness of the printed cathode, 3 μm, was hardly a tenth of the conventional ones (30 and 32 μm for the painted and double layer cathodes), which is more than enough to explain the discrepancy in PPD (110 mW cm<sup>-2</sup>).<sup>[99]</sup> Furthermore, the cell with only a painted layer achieved a PPD of only 540 mW cm<sup>-2</sup>, which is a much larger drop from the double layer cathode's performance than would be expected due to the thickness difference.

In 2015, Li et al. reported on the performance of an inkjet-printed SDC–SSC cathode, supported on a tape-cast NiO–YSZ anode with a YSZ electrolyte and GDC buffer layer deposited by wet powder spraying.<sup>[105]</sup> Their inkjet-printed cell achieved a PPD of 550 mW cm<sup>-2</sup> at 750 °C with pure H<sub>2</sub>, which increased to 940 mW cm<sup>-2</sup> when they added 10 wt% of pore former (PEG-4000) to the ink. However, the cathode prepared by conventional spraying, for comparison, performed better than either of the printed ones (PPD 1150 mW cm<sup>-2</sup>).

In 2016, Han et al. printed LSCF cathodes using an HP Deskjet 1010 printer and tested the effect of image brightness and luminosity, when printing in grayscale, on the architecture and performance of the electrode.<sup>[100]</sup> Besides the cathode, their cells consisted of NiO–YSZ anode-supports (uniaxial pressing), YSZ electrolytes (10 μm, screen printing), and GDC buffer (200 nm, pulsed layer deposition) layers. While there was no clear trend in regards to the porosity of the films, it was found that intermediate values of luminosity during printing (100 to 150) gave thicker electrodes (≈5 μm) and significantly better performance (350–377 mW cm<sup>-2</sup> at 600 °C) with humidified H<sub>2</sub> fed to the anode and synthetic air (20% O<sub>2</sub>) to the cathode. Lower values of luminosity deposited thicker layers per pass and resulted in large cracks in the cathode surface. Higher values of luminosity deposited less ink per pass and gave much thinner electrodes with a PPD of 319 mW cm<sup>-2</sup> at 600 °C (with the same anode and cathode feed flow).

The following year, they also prepared a GDC ink and used two of the printer's cartridges to print a 900 nm GDC buffer layer and composite LSCF–GDC cathodes, this time on a spin-coated YSZ electrolyte.<sup>[101,102]</sup> Testing the corresponding SOFCs at 650 °C with humidified H<sub>2</sub> and synthetic air showed that a 50:50 LSCF to GDC ratio and an electrode thickness of 14 μm gave the highest PPD of 574 mW cm<sup>-2</sup>, while with thinner (8 μm) cathodes a 70:30 ratio was the most effective (349 mW cm<sup>-2</sup>). Finally, in 2020, this group produced a fully inkjet-printed, anode-supported cell using a newer printer and suspension inks of commercial component nanopowders.<sup>[102]</sup> Specifically, their cell consisted of a die-pressed NiO–YSZ support onto which were successively printed a NiO–YSZ interlayer (6 μm), a dense YSZ layer (0.8 μm), a GDC buffer (0.5 μm), and a PBSCF cathode (8 μm). The anode and electrolyte were cosintered at 1400 °C, the buffer layer was sintered at 1200 °C and the cathode at 900 °C for 3, 2, and 3 h, respectively. The

purpose of the anode interlayer was to reduce the pore size of the NiO–YSZ support and prevent the deformation of the thin electrolyte layer. With humidified H<sub>2</sub> and air fed to the anode and cathode, respectively, this cell achieved an OCV of 1.14 V and a PPD of 730 mW cm<sup>-2</sup>, at 650 °C. The overall ASR at this temperature was ≈1.5 Ω cm<sup>-2</sup>, while the ohmic contribution was 0.05 Ω cm<sup>-2</sup>.

More recently, two different groups used inkjet printing to fabricate composite electrodes.<sup>[134,154]</sup> In the first, the authors used a solvothermal method to prepare Ag@SDC core-shell nanoparticles, which they then used in the formulation of an organic-based printable ink.<sup>[134]</sup> Their anodes (3 μm sintered thickness) were deposited on commercial SDC pellets (300 μm thick) and the cells were completed by radio frequency sputtered Pt anodes. These cells achieved an OCV of about 1.05 V and a PPD of 56 mW cm<sup>-2</sup> at 450 °C under dry H<sub>2</sub>. The corresponding impedance spectra revealed an ohmic resistance of 3.5 Ω cm<sup>-2</sup> and an overall ASR of 4.35 Ω cm<sup>-2</sup>. The authors compared this cell to one with plane Ag nanoparticles printed as the cathode, and found a clear superiority of the composite material over plain Ag in terms of both performance and stability.<sup>[134]</sup> The second group deposited symmetrical NiO–SDC electrodes (15–25 μm thick) on commercial ScCeSZ electrolyte pellets by either inkjet or screen printing.<sup>[154]</sup> After sintering and reduction, they examined the performance of these electrodes under dry H<sub>2</sub> at several temperatures between 600 and 800 °C by analyzing electrochemical impedance data. They found that the polarization resistance of the screen-printed electrodes was about five times that of the inkjet-printed ones in this temperature range (e.g., 2.3 vs 0.43 Ω cm<sup>-2</sup> at 800 °C).<sup>[154]</sup>

### 6.3. SOFC Performance Studies with Inkjet-Infiltrated Electrodes

This section deals with publications focusing on the infiltration via inkjet printing of various inks into previously sintered electrodes, rather than printing onto a flat electrolyte or buffer layer. The potential benefits of this method are discussed later on in Section 7.

The earliest of these works involved a NiO–YSZ anode (38 μm) painted onto a 10 mol% Sc<sub>2</sub>O<sub>3</sub>–1 mol% CeO<sub>2</sub>–ZrO<sub>2</sub> (ScCeSZ) electrolyte (0.3 mm) and sintered at 1400 °C.<sup>[157]</sup> A BZY precursor solution was then infiltrated by either micropipette or by IJP, at weight ratios of 1, 3 or 6:100, followed by sintering at 1300 °C. The cell was completed by painting an LSM–ScCeSZ, cathode on the other side of the electrolyte. Fuel cell measurements were carried out at 900 °C under either 3% humidified H<sub>2</sub> or dry CH<sub>4</sub>, fed at a rate of 200 mL min<sup>-1</sup>, while oxygen was fed to the cathode at 60 mL min<sup>-1</sup>. With the first fuel, both the 1 and 3:100 ratio electrodes gave similar performances (790 mW cm<sup>-2</sup>), while under CH<sub>4</sub> feed the electrode with the 3:100 ratio performed best (650 mW cm<sup>-2</sup>). The authors found that further increasing the amount of infiltrated BZY (to a 6:100 ratio) had a detrimental effect on performance, with this electrode yielding a lower PPD than non-infiltrated NiO–YSZ with both fuels, and attributed this to a decrease in TPB. Finally, they reported that the electrode infiltrated by micropipette performed similarly to the worst inkjet infiltrated ones.<sup>[157]</sup>

In 2016, Tomov et al. studied the effect of substituting GDC for YSZ in NiO-based anodes and of Co-infiltration on LSM inkjet-printed electrodes in symmetrical cells.<sup>[128]</sup> They found that by increasing the GDC content of the anode the polarization resistance was reduced, with the overall ASR dropping from 32 (pure YSZ) to 15 (pure GDC)  $\Omega \text{ cm}^{-2}$ , in symmetrical cells under 4%  $\text{H}_2/\text{Ar}$  at 800 °C. When a  $\text{Co}(\text{NO}_3)_2$  ink was infiltrated on presintered LSM symmetrical electrodes, the overall ASR, under air, dropped from 7 to 4  $\Omega \text{ cm}^{-2}$  at 800 °C.

In a following publication, the same group tested the inkjet infiltration of GDC into the NiO–YSZ anode-support ( $\approx 0.5$  mm thickness) of commercial cells with both a water- and a PPA-based precursor ink.<sup>[151]</sup> Due to the high density of the sintered (at 1400 °C) anode it was only possible to add about 1 wt% of GDC and the effect was expectedly marginal, with all cells exhibiting PPDs around 70  $\text{mW cm}^{-2}$  at 650 °C. They then prepared symmetrical cells with inkjet-printed NiO–GDC electrodes (10  $\mu\text{m}$  thickness) on GDC electrolytes, sintered at only 1100 °C. Here they managed to infiltrate up to 30 wt% GDC with the PPA ink, after which the cells were sintered at 1400 °C. The polarization resistance of the infiltrated symmetrical cells compared to the non-infiltrated one was found to decrease by about an order of magnitude at 600 °C under humidified  $\text{H}_2$ .

They also tested the infiltration of composite, LSCF–GDC cathodes with the same GDC precursor inks.<sup>[130]</sup> The electrodes were inkjet-printed (suspension inks) symmetrically onto GDC electrolytes/supports and the infiltration resulted in lower cell impedances in all cases, but was more effective in electrodes with lower GDC loading. In particular, the overall ASRs at 550 °C under ambient air dropped from 42 to 22  $\Omega \text{ cm}^{-2}$  when infiltrating 60:40 LSCF–GDC electrodes, but only from 19 to 15  $\Omega \text{ cm}^{-2}$  when infiltrating with a 40:60 composition.

The last study involving inkjet infiltration was by Venezia et al. and reported on the infiltration of GDC or LSC precursor inks into LSCF electrodes.<sup>[150]</sup> After testing these modifications on symmetrical inkjet-printed electrodes, they infiltrated the cathodes of commercial NiO–GDC|YSZ|LSCF cells (30  $\mu\text{m}$  thick electrodes). The test with symmetrical cells showed improved electrode stability (72 h), through the suppression of Sr migration (slightly better for GDC than LSC). On the other hand, the fuel cell tests showed improved performance in terms of PPD and impedance, especially for LSC. Specifically, the non-infiltrated reference cathode exhibited a PPD of 250  $\text{mW cm}^{-2}$ , the GDC infiltrated one resulted in 310  $\text{mW cm}^{-2}$ , and the LSC infiltrated one achieved 350  $\text{mW cm}^{-2}$ . The corresponding polarization ASR dropped from  $\approx 1.6 \Omega \text{ cm}^{-2}$  to 0.6 and 0.4  $\Omega \text{ cm}^{-2}$ , respectively, while the ohmic contribution of the cells with infiltrated cathodes was about half that of the reference cell, attributed to the increased ionic conductivity of these cathodes.

## 7. Challenges and Perspectives

In this review, we have summarized the recent achievements on inkjet-printed SOFCs concerning ink development of active materials, inkjet deposition of electrolytes and electrodes, and electrochemical performance of printed cells.

So far, inkjet printing has been established as a promising deposition technique for manufacturing of planar SOFC single cells, utilizing different ink development methods. Most of the inks developed utilize ex situ/suspension procedures, with more than half of the total inkjet-printed SOFC publications using organic solvent-based inks. This methodology is regarded to be the most flexible in terms of solvent and additives used, as well as more compatible with traditional contact-based deposition techniques that utilize pastes of similar compositions. In regards to water-based ink development either for ex situ or in situ inks, additional effort should follow in order to establish stable and easy to formulate inkjet-printable inks for all SOFC components.

Another important remark is the fact that the majority of these IJP studies utilize homogenization methods, from low intensity grinding, ultrasonic treatment, to mostly low intensity but long duration ball milling, in order to achieve better suspension stability of ex situ inks and reduce particle polydispersity prior to printing. It would be interesting for future works to explore the implementation of such homogenization methods in early stage crystal growth of in situ inks. It would also be interesting to reduce the inkjet ink development and homogenization processes to a single-step of synthesis and fabrication, e.g., by utilizing CHFS and ball milling processes in-line.

Even though fully inkjet-printed SOFCs are deemed achievable, the vast majority of the reports in this review present partially printed devices rather than fully printed, highlighting the novelty of the field. Moreover, all the available studies report on inkjet-printed planar SOFC single cells, while to the best of our knowledge there are no works in literature dealing with tubular cells or planar/tubular SOFC stacks. This is probably the case, because IJP is commonly regarded as a 2D-printing technique, even though there have been limited reports on utilizing IJP coating, patterning on the fabrication of 3D structures in different application fields.<sup>[158–162]</sup> We believe that, similarly to other fields of inkjet printing application, future studies will be focused on fully printed devices, as is the case for very few publications presented here. By establishing this methodology, later works are expected to move toward IT- and LT-fully printed SOFCs, mainly with planar but also with tubular geometry, with various materials apart from the conventional ones that have mostly been tested so far. A change in cell configuration could be explored as well. Even though the electrode-supported one is estimated to be more prevalent due to the higher achieved electrochemical performance, a trend toward metal-supported cells is illustrated by the studies reported in this review. Either case seems more preferable than the electrolyte-supported cells, since printing a cell bottom-up facilitates implementation on scale-up manufacturing of fully printed SOFCs, especially in the case of layer-by-layer fabrication such as in IJP.

Additionally, a number of the articles mentioned in this review explore the possibility of implementing inkjet printing for the infiltration of active materials on previously deposited electrodes. This methodology makes the fabrication process more complicated, with additional steps, in order to improve the device performance and durability. In general, Ni infiltration on YSZ scaffolds for anode preparation has been shown to minimize the degradation impact from Ni volume expansion during redox cycling,<sup>[163]</sup> which can have multiple benefits since

degradation not only mechanically compromises the anode layer but reduces the TPB, lowering the achieved SOFC performance.<sup>[164]</sup> By infiltrating electrocatalytically active materials on SOFC electrodes, additional TPB sites could be introduced in the electrode films. Thus, compromising by applying an extra fabrication step in order to optimize the material properties, can be beneficial to achieve better cell performances and higher power densities. This benefit is showcased by publications on inkjet infiltrated SOFCs in this review, but unfortunately authors do not provide a comparison between infiltrated electrodes and conventional ones with equivalently higher amount of the infiltrated material in bulk. Such a comparison would be interesting to report in order to experimentally establish the impact of the infiltration procedure specifically with inkjet printing, as well as to quantify the impact of bulk material increase. Similar novel features on the manufacturing process of SOFCs can be expected in the future, since the implementation of additive manufacturing, and in particular inkjet printing, can expand SOFC single cell and stack fabrication.

It is also worth mentioning that recent progress on inkjet-printed SOFCs is not limited to electrolyte and electrode materials deposition. A notable example is the report of Pandiyan et al., who recently reported on the inkjet printing of spinel-based protective layer coatings for SOFC interconnects, using water-based inks.<sup>[165]</sup> Although it is of high interest, discussion of such reports goes beyond the scope of this review, thus readers are encouraged to refer to the original publication for details. Another thing that is prevalent from state-of-the-art on inkjet-printed SOFCs is that literature is mostly limited to oxygen conducting SOFCs, and rarely expands on proton conducting SOFCs, which were also deemed to be beyond the scope of this review.

Such rare examples of proton conducting inkjet-printed SOFCs are the publications of Da'as et al. on impregnation by inkjet of LSM onto BZY, making them the first group to apply inkjet printing to proton conducting solid oxide fuel cells (PCFCs).<sup>[166]</sup> Their infiltrated cathodes, supported on a NiO-BZY/BZY anode-electrolyte bilayer, were fed with humidified H<sub>2</sub>, and achieved an OCV of ≈0.95 V and a PPD of 200 mW cm<sup>-2</sup> at 600 °C. The latter was more than an order of magnitude higher than that obtained in a similar cell with a cathode prepared from a mechanical mixture of LSM and BZY powders, and demonstrates the potential of inkjet printing methods for PCFC fabrication. Another such case is the recent publication by Park et al.<sup>[167]</sup> where the authors utilized inkjet deposition of PBSCF, similarly to their previously reported works,<sup>[100,101]</sup> to fabricate a PCFC with a Pd rich interface layer between the electrolyte and cathode layers, and improve the performance of cells. As the interest of researchers in PCFCs is increasing, more works implementing inkjet printing for their manufacturing are to be expected.

In regards to the performance of the inkjet-printed SOFCs analyzed in this review, less than half of the publications report on fuel cell testing and EIS measurements, making this field better established in regards to its manufacturing prospects, but less rich in regards to printed device implementation. Little work is available on partially or fully inkjet-printed devices in order to establish the advertised advantages of this fabrication

method in SOFC fabrication and to compare between different manufacturing methods. However, presented reports are encouraging, with authors achieving more precise control of device layer thickness, which lead to better performance of devices, especially at lower temperatures. Increased performance at lower temperatures by reducing layer thickness of SOFCs is a known behavior, which is being exploited by controlled deposition techniques such as inkjet printing. Moreover, publications reporting on inkjet-printed device performance are mostly focused on the use of hydrogen fuel, apart from just two publications presenting DC-SOFCs, with carbon produced from the radio frequency plasma splitting of methane as fuel source.

While there are a multitude of studies on the preparation of inks and the tuning of their physicochemical properties within printable ranges, there are relatively few publications which report on the performance of the printed element itself or for the whole cell. It is, therefore hard to draw concrete conclusions, let alone find statistically significant variations with respect to the type of ink or the printing parameters. Of the top five PPDs reported, four were obtained by using inks with water as the solvent, while the other involved inks with a mixture of water and ethanol and four out of these five studies used suspension inks. This might indicate that aqueous suspension inks could be the method of choice for inkjet-printed SOFCs, in regards to electrochemical performance.

However, the situation is rather more complicated and other parameters must also be taken into account when comparing performance. The most important of these are the electrolyte thickness (PPD decreases with higher electrolyte thickness) and the operating temperature of the SOFC (PPD increases as temperature rises). For instance, the highest PPD (1.5 W cm<sup>-2</sup>) was obtained at 800 °C,<sup>[103]</sup> while the next two (≈1 and 0.75 W cm<sup>-2</sup>) were obtained at 750 °C.<sup>[104,105]</sup> Furthermore, the two highest PPDs were reported on cells with printed electrolytes (thickness <10 μm),<sup>[103,104]</sup> while the third highest was obtained with a printed cathode layer on a tape-cast electrolyte (50 μm thick).<sup>[105]</sup> Other parameters such as the electrode materials, their thickness and the deposition method, as well as the presence or not of an interlayer further add to the complexity of comparing the different IJP SOFC performance studies. Finally, the type of fuel, the flow rate and/or concentration of fuel and oxidant over the respective electrodes must also be taken into account when comparing the performance of different cells.

This complexity is illustrated in **Figure 12**, where the reported PPDs are plotted against the electrolyte thickness (a) and operating temperature (b). While a general trend of increase with temperature and decrease with thickness may be observed, there is little evidence of a strong correlation between power density and these important parameters. In fact, for some parameter values, there is considerable variance in the obtained PPDs even at the same temperature or thickness.

Moreover, reported data on comparison of performance for cells with inkjet-printed components versus cells fabricated by other deposition methods is even more limited. Of the 26 works presented in Table 1, only 7 compare cells with inkjet-printed components with cells of conventional deposition methods, and even so, there is rarely a clear advantage of one method over the other. For instance, in one work comparing cathodes

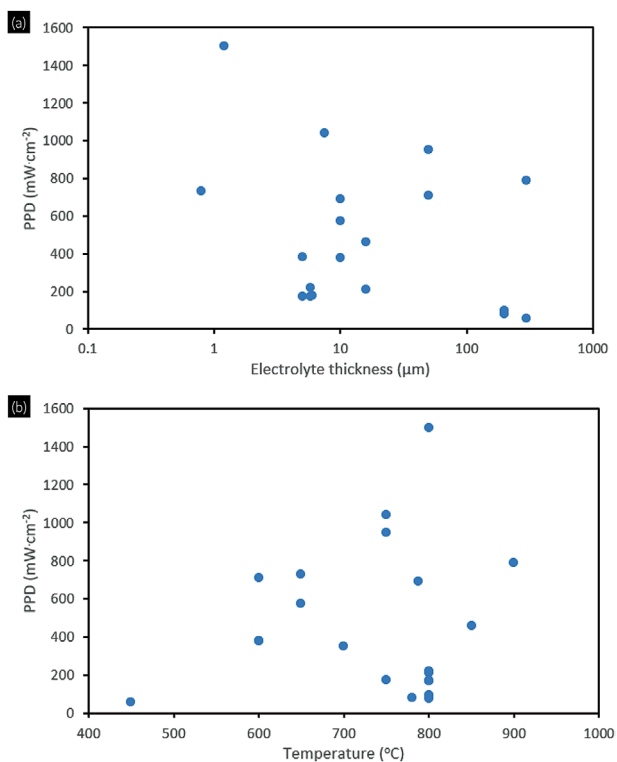


**Figure 12.** Reported PPDs for fuel cells with at least one inkjet-printed component in regards to a) electrolyte thickness and b) operating temperature.

prepared by wet powder spraying and inkjet printing, the difference in terms of PPD at  $750^{\circ}\text{C}$  was about 10%, in favor of the former.<sup>[105]</sup> There is also one work studying symmetrical cells, wherein the IJP electrodes had much lower polarization resistance than the screen printed ones between  $600$  and  $800^{\circ}\text{C}$ .<sup>[154]</sup> However, in most cases inkjet-printed electrodes have the advantage over conventional ones when operation temperature is low or intermediate ( $<750^{\circ}\text{C}$ ),<sup>[99,110,112,156]</sup> while this difference fades as the temperature increases.<sup>[110,112,124]</sup> Thus, a more systematic experimental approach is required to assess the advantages of IJP technology for SOFC fabrication over other conventional approaches, while techno-economic and life cycle assessment studies will add to this comparison.

## 8. Concluding Remarks

Solid oxide fuel cells have been reported by various authors to be fabricated by the inkjet printing deposition technique, either by partial printing of individual cell components or by fully inkjet-printed SOFCs. The field is quite unexplored in regards to IJP SOFC electrochemical performance and its comparison with conventional fabrication techniques. However, in the fabrication and technology implementation aspect a great effort has been made with different methodologies on ink development, printing optimization and characterization of inkjet-printed films. In conclusion, some major research highlights presented in this review on IJP of SOFCs are given below.

- An emphasis on the analysis of ink development and characterization is prevalent, in order to establish the stability and jettability of inkjet inks. Ex situ ink development seems to be favorable in literature over in situ inks, due to the flexibility it provides on ink formulation, with a preference on organic-based solvents, while the use of homogenization techniques such as ball milling is largely employed.
- Materials used are mostly suitable for HT- and IT-SOFCs, however since IJP enables deposition of thin films as SOFC components it is estimated that a trend toward mainly IT- and LT-SOFCs will be established. Partially printed cells are manufactured in the majority of this literature, while few novel papers report on fully printed cells focusing on planar geometry, with a preference on electrode- or metal-supported configurations, over the electrolyte-supported, due to the ease for bottom-up layer-by-layer fabrication. Also, implementation of IJP in this field is not restricted to thin film deposition of the SOFCs components, and expands on material infiltration, mostly in electrode layers, but with limited comparison reported to establish the actual usefulness of this process in the case of IJP fabrication of SOFCs.
- Few of the works analyzed in this review report on the electrochemical performance of inkjet-printed SOFCs, most of which utilize hydrogen fuel. Results indicate better performance of cells on intermediate temperatures, with the two highest PPDs of  $1.5$  and  $1\text{ W cm}^{-2}$  achieved at  $800$  and  $750^{\circ}\text{C}$ , respectively. Since literature on cell performance is lacking, a clear association between cell PPDs, operational temperature, and film thickness cannot be drawn yet. Additionally, reports comparing the effect of the fabrication technique on cell performance is too limited to reach any valid conclusions. The only evident advantage of IJP over deposition by conventional methods, for similar SOFCs components, is an enhanced performance in the case of lower operating temperatures.

To the best of the authors' knowledge this novel field, due to its inherent advantages associated with the benefits of additive manufacturing, is expected to grow in interest, with a focus mainly on deposition of novel materials for low and intermediate temperature SOFCs, as well as on PCFCs, and on fully inkjet-printed cells and stacks, employing different geometries and configurations. A successful implementation of inkjet printing in SOFCs could definitely assist in their wider deployment in real scale applications and marketization, by accelerating manufacturing times and lowering manufacturing costs, while enabling easier design prototyping and precise deposition of features in the nanoscale.

## Supporting Information

Supporting Information is available from the Wiley Online Library or from the author.

## Acknowledgements

This work was financially supported in part by the Stavros Niarchos Foundation within the framework of the project ARCHERS ("Advancing

Young Researchers' Human Capital in Cutting Edge Technologies in the Preservation of Cultural Heritage and the Tackling of Societal Challenges"). This research was cofinanced by the European Union and Greek national funds through the Operational Program Competitiveness, Entrepreneurship and Innovation, under the call RESEARCH – CREATE – INNOVATE (Project Code: T1EDK-01894).

## Conflict of Interest

The authors declare no conflict of interest.

## Keywords

additive manufacturing, electrochemical performance, inkjet printing, solid oxide fuel cells, thin films

Received: November 9, 2021

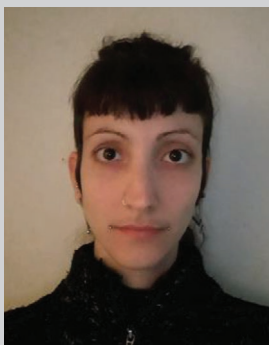
Revised: January 15, 2022

Published online:

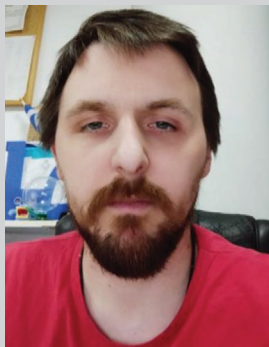
- [1] Organisation for Economic Co-operation and Development (OECD)/International Energy Agency (IEA), *Key World Energy Statistics 2014*, OECD, Paris **2014**.
- [2] V. E. Pareto, M. P. Pareto, *SSRN Electron. J.* **2008**, <https://ssrn.com/abstract=1221622> (accessed: August 2008).
- [3] Our world in data, "Share of electricity production from fossil fuels, World," <https://ourworldindata.org/grapher/share-of-electricity-production-from-fossil-fuels> (accessed: May 2020).
- [4] Organisation for Economic Co-operation and Development (OECD)/International Energy Agency (IEA), *World Energy Outlook 2016*, OECD, Paris **2016**.
- [5] P. Griffin, *The Carbon Majors Database CDP: Carbon Majors Report*, **2017**.
- [6] M. Tahir, N. S. Amin, *Renewable Sustainable Energy Rev.* **2013**, *25*, 560.
- [7] UNFCCC: *Conference of the Parties (COP), Adoption of the Paris Agreement, Proposal by the President*, **2015**.
- [8] EU-Commission, *Europe's 2030 Climate and Energy Targets*, **2021**.
- [9] V. Masson-Delmotte, P. Zhai, A. Pirani, S. L. Connors, C. Péan, S. Berger, C. Péan, N. Caud, Y. Chen, L. Goldfarb, M. I. Gomis, H. Huang, K. Leitzell, E. Lonnoy, J. B. R. Matthews, T. K. Maycock, T. Waterfield, O. Yelekçi, R. Yu, B. Zhou, IPCC, *Climate Change 2021: Summary for Policymakers*, Cambridge University, Unpublished.
- [10] J. Larminie, A. Dicks, *Fuel Cell Systems Explained*, John Wiley & Sons, Ltd, West Sussex, England **2003**.
- [11] N. Mahato, A. Banerjee, A. Gupta, S. Omar, K. Balani, *Prog. Mater. Sci.* **2015**, *72*, 141.
- [12] V. S. Bagotsky, *Fuel Cells*, John Wiley & Sons, Inc., Hoboken, NJ, USA **2012**, pp. 133–157.
- [13] A. Hammou, *Advances in Electrochemical Science and Engineering*, Wiley, New York **1991**, pp. 87–139.
- [14] U.S. Department of Energy, "Energy Department Invests \$13.5M to Advance Solid Oxide Fuel Cell Technology," can be found under <https://www.energy.gov/fe/articles/energy-department-invests-135m-advance-solid-oxide-fuel-cell-technology> (accessed: XX 2018).
- [15] CHIC *European Fuel Cell Bus Project Final Report*, **2016**.
- [16] B. Andresen, A. Norheim, J. Strand, Ø. Ulleberg, A. Vik, I. Wærnhus, *Energy Proc.* **2014**, *63*, 279.
- [17] S. A. Nabavi, M. Erans, V. Manović, *Appl. Energy* **2019**, *255*, 113731.
- [18] VTT Technical Research Centre of Finland Ltd, *Final Report Summary – LARGE-SOFC (Towards a Large SOFC Power Plant)*, **2009**.
- [19] M. Gandiglio, A. Lanzini, M. Santarelli, M. Aciri, T. Hakala, M. Rautanen, *Int. J. Hydrogen Energy* **2020**, *45*, 5449.
- [20] M. Santarelli, *Final Report Summary – SOFCOM (SOFC CCHP with Poly-Fuel: Operation and Maintenance)*, **2015**.
- [21] K. Yamaji, T. Ishiyama, K. D. Bagarinao, H. Kishimoto, T. Horita, H. Yokokawa, *ECS Trans.* **2017**, *78*, 2337.
- [22] DESTA-Project, *Final Report Summary – DESTA (Demonstration of 1st European SOFC Truck APU)*, **2015**.
- [23] L. S. Mahmud, A. Muchtar, M. R. Somalu, *Renewable Sustainable Energy Rev.* **2017**, *72*, 105.
- [24] J. C. Ruiz-Morales, A. Tarancón, J. Canales-Vázquez, J. Méndez-Ramos, L. Hernández-Afonso, P. Acosta-Mora, J. R. Marín Rueda, R. Fernández-González, *Energy Environ. Sci.* **2017**, *10*, 846.
- [25] X. Y. Tai, A. Zhakeyev, H. Wang, K. Jiao, H. Zhang, J. Xuan, *Fuel Cells* **2019**, *19*, 636.
- [26] Z. Chen, Z. Li, J. Li, C. Liu, C. Lao, Y. Fu, C. Liu, Y. Li, P. Wang, Y. He, *J. Eur. Ceram. Soc.* **2019**, *39*, 661.
- [27] S. P. S. Badwal, S. Giddey, C. Munnings, A. Kulkarni, *J. Australas. Ceram. Soc.* **2014**, *50*, 23.
- [28] V. S. Bagotsky, A. M. Skundin, Y. M. Volkovich, *Electrochemical Power Sources*, John Wiley & Sons, Inc., Hoboken, NJ, USA **2015**, pp. 199–212.
- [29] S.-M. Ho, *Mater. Sci. Eng.* **1982**, *54*, 23.
- [30] J.-P. P. Brog, C.-L. L. Chanez, A. Crochet, K. M. Fromm, *RSC Adv.* **2013**, *3*, 16905.
- [31] S. Zhuyikov, *Electrochemistry of Zirconia Gas Sensors*, CRC Press, Boca Raton, FL **2007**.
- [32] A. M. Abdalla, S. Hossain, A. T. Azad, P. M. I. Petra, F. Begum, S. G. Eriksson, A. K. Azad, *Renewable Sustainable Energy Rev.* **2018**, *82*, 353.
- [33] J. P. P. Huijsmans, F. P. F. Van Berkel, G. M. Christie, *J. Power Sources* **1998**, *71*, 107.
- [34] M. Li, Y. Zhang, M. An, Z. Lü, X. Huang, J. Xiao, B. Wei, X. Zhu, W. Su, *J. Power Sources* **2012**, *218*, 233.
- [35] *Fuel Cell Technologies: State and Perspectives* (Eds: N. Sammes, A. Smirnova, O. Vasylyev), Springer, Berlin **2005**.
- [36] S. P. S. Shaikh, A. Muchtar, M. R. Somalu, *Renewable Sustainable Energy Rev.* **2015**, *51*, 1.
- [37] E. Gagaoudakis, G. Michail, V. Kampylafka, K. Tsagaraki, E. Aperathitis, K. Moschovis, V. Binas, G. Kiriakidis, *Sens. Lett.* **2017**, *15*, 663.
- [38] I. Hotovy, J. Huran, L. Spiess, S. Hascik, V. Rehacek, *Sens. Actuators, B* **1999**, *57*, 147.
- [39] R. S. Kate, S. A. Khalate, R. J. Deokate, *J. Alloys Compd.* **2018**, *734*, 89.
- [40] B. Iwanschitz, J. Sfeir, A. Mai, M. Schütze, *J. Electrochem. Soc.* **2010**, *157*, B269.
- [41] C. G. Granqvist, *Thin Solid Films* **2014**, *564*, 1.
- [42] K. Sato, H. Abe, T. Misono, K. Murata, T. Fukui, M. Naito, *J. Eur. Ceram. Soc.* **2009**, *29*, 1119.
- [43] M. Pihlatie, A. Kaiser, M. Mogensen, *Solid State Ionics* **2009**, *180*, 1100.
- [44] D. Fouquet, A. C. Müller, A. Weber, E. Ivers-Tiffée, *Ionics* **2003**, *9*, 103.
- [45] C. Sun, R. Hui, J. Roller, *J. Solid State Electrochem.* **2010**, *14*, 1125.
- [46] D. Rembelski, J. P. Viricelle, L. Combemale, M. Rieu, *Fuel Cells* **2012**, *12*, 256.
- [47] C. L. Chang, C. S. Hsu, J. B. Huang, P. H. Hsu, B. H. Hwang, *J. Alloys Compd.* **2015**, *620*, 233.
- [48] L. Jiang, T. Wei, R. Zeng, W.-X. Zhang, Y.-H. Huang, *J. Power Sources* **2013**, *232*, 279.
- [49] S. Ramanathan, *Thin Film Metal-Oxides*, Springer, Boston, MA **2010**.

- [50] H. J. Hwang, J. W. Moon, S. Lee, E. A. Lee, *J. Power Sources* **2005**, *145*, 243.
- [51] E. Zhao, Z. Jia, L. Zhao, Y. Xiong, C. Sun, M. E. Brito, *J. Power Sources* **2012**, *219*, 133.
- [52] L. Fan, Y. Wang, Z. Jia, Y. Xiong, M. E. Brito, *Ceram. Int.* **2015**, *41*, 6583.
- [53] M. Li, K. Chen, B. Hua, J. Luo, W. D. A. Rickard, J. Li, J. T. S. Irvine, S. P. Jiang, *J. Mater. Chem. A* **2016**, *4*, 19019.
- [54] Z. Zakaria, Z. Awang Mat, S. H. Abu Hassan, Y. Boon Kar, *Int. J. Energy Res.* **2020**, *44*, 594.
- [55] M. Z. Khan, A. Iltaf, H. A. Ishfaq, F. N. Khan, W. H. Tanveer, R.-H. Song, M. T. Mehran, M. Saleem, A. Hussain, Z. Masaud, *J. Asian Ceram. Soc.* **2021**, *9*, 745.
- [56] V. V. Krishnan, *Wiley Interdiscip. Rev.: Energy Environ.* **2017**, *6*, 246.
- [57] S. P. S. Badwal, K. Foger, *Ceram. Int.* **1996**, *22*, 257.
- [58] M. R. Somalu, A. Muchtar, W. R. W. Daud, N. P. Brandon, *Renewable Sustainable Energy Rev.* **2017**, *75*, 426.
- [59] L. C. Hwa, S. Rajoo, A. M. Noor, N. Ahmad, M. B. Uday, *Curr. Opin. Solid State Mater. Sci.* **2017**, *21*, 323.
- [60] F. Zhang, M. Wei, V. V. Viswanathan, B. Swart, Y. Shao, G. Wu, C. Zhou, *Nano Energy* **2017**, *40*, 418.
- [61] A. Pesce, A. Hornés, M. Núñez, A. Morata, M. Torrell, A. Tarancón, *J. Mater. Chem. A* **2020**, *8*, 16926.
- [62] L. J. Deiner, T. L. Reitz, *Adv. Eng. Mater.* **2017**, *19*, 1600878.
- [63] V. J. Ferreira, D. Wolff, A. Hornés, A. Morata, M. Torrell, A. Tarancón, C. Corchero, *Appl. Energy* **2021**, *291*, 116803.
- [64] MordorIntelligence, *Inkjet Printing Market – Growth, Trends, Forecasts (2020–2025)*, Mordor Intelligence, Hyderabad India **2019**.
- [65] MarketResearchEngine, *Inkjet Printing Technologies Market Research Report – Global Forecast 2020–2025*, Market Research Engine, Deerfield Beach, US **2020**.
- [66] M. Singh, H. M. Haverinen, P. Dhagat, G. E. Jabbour, *Adv. Mater.* **2010**, *22*, 673.
- [67] S. D. Hoath, *Fundamentals of Inkjet Printing*, Wiley-VCH, Weinheim, Germany **2016**.
- [68] P. Calvert, *Chem. Mater.* **2001**, *13*, 3299.
- [69] M. Gao, L. Li, Y. Song, *J. Mater. Chem. C* **2017**, *5*, 2971.
- [70] R. Martinez-Duarte, *Electrophoresis* **2012**, *33*, 3110.
- [71] J. Perelaer, U. S. Schubert, *Polymer Science A: Comprehensive Reference*, Elsevier, Amsterdam **2012**, pp. 147–175.
- [72] J. K. Fink, *The Chemistry of Printing Inks and Their Electronics and Medical Applications*, John Wiley & Sons, Inc., Hoboken, NJ, USA **2014**.
- [73] H. Wijshoff, *Phys. Rep.* **2010**, *491*, 77.
- [74] R. Rioboo, C. Tropea, M. Marengo, *Atomization Sprays* **2001**, *11*, 12.
- [75] H. Wijshoff, *Curr. Opin. Colloid Interface Sci.* **2018**, *36*, 20.
- [76] M. J. Rosen, *Surfactants and Interfacial Phenomena*, John Wiley & Sons, Inc., Hoboken, NJ, USA **2004**.
- [77] A. J. Bard, L. R. Faulkner, *Printing on Polymers*, Elsevier, New York **2016**.
- [78] X. Zhang, S. Yu, Z. He, Y. Miao, *Surf. Rev. Lett.* **2004**, *11*, 7.
- [79] D. Li, W.-Y. Lai, Y.-Z. Zhang, W. Huang, *Adv. Mater.* **2018**, *1704738*, 1704738.
- [80] K. S. Lee, N. Ivanova, V. M. Starov, N. Hilal, V. Dutschk, *Adv. Colloid Interface Sci.* **2008**, *144*, 54.
- [81] D. Pesach, A. Marmur, *Langmuir* **1987**, *3*, 519.
- [82] L. Cui, J. Zhang, X. Zhang, L. Huang, Z. Wang, Y. Li, H. Gao, S. Zhu, T. Wang, B. Yang, *ACS Appl. Mater. Interfaces* **2012**, *4*, 2775.
- [83] R. D. Deegan, O. Bakajin, T. F. Dupont, G. Huber, S. R. Nagel, T. A. Witten, *Nature* **1997**, *389*, 827.
- [84] J. A. Lim, W. H. Lee, H. S. Lee, J. H. Lee, Y. D. Park, K. Cho, *Adv. Funct. Mater.* **2008**, *18*, 229.
- [85] S. Magdassi, A. Kamyshny, Y. Shacham-Diamand, *Nanomaterials for 2D and 3D Printing*, Wiley-VCH, Weinheim, Germany **2017**.
- [86] S. Wünscher, R. Abbel, J. Perelaer, U. S. Schubert, *J. Mater. Chem. C* **2014**, *2*, 10232.
- [87] *Microw. Opt. Technol. Lett.* **2016**, *58*, 2884.
- [88] L. Xie, M. Mäntysalo, A. L. Cabezas, Y. Feng, F. Jonsson, L.-R. Zheng, *Mater. Lett.* **2012**, *88*, 68.
- [89] A. A. Castrejón-Pita, J. R. Castrejón-Pita, I. M. Hutchings, *Phys. Rev. Lett.* **2012**, *108*, 074506.
- [90] J. E. Fromm, *IBM J. Res. Dev.* **1984**, *28*, 322.
- [91] N. Reis, C. Ainsley, B. Derby, *J. Appl. Phys.* **2005**, *97*, 094903.
- [92] A. Marmur, H. Dodiuk, D. Pesach, *J. Adhes.* **1987**, *24*, 139.
- [93] B.-J. de Gans, U. S. Schubert, *Langmuir* **2004**, *20*, 7789.
- [94] R. D. J. Nelson, *Dispersing Powders in Liquids*, Elsevier Science, New York **1988**.
- [95] W. Zapka, *Handbook of Industrial Inkjet Printing*, Wiley-VCH Verlag GmbH & Co. KGaA, Weinheim, Germany, **2017**.
- [96] W. Wu, *Nanoscale* **2017**, *9*, 7342.
- [97] M. Fang, W. Voit, Y. Wu, L. Belova, K. V. Rao, *MRS Online Proc. Libr.* **2013**, *1547*, 13.
- [98] S. Magdassi, *The Chemistry of Inkjet Inks*, World Scientific, Singapore **2009**.
- [99] N. Yashiro, T. Usui, K. Kikuta, *J. Eur. Ceram. Soc.* **2010**, *30*, 2093.
- [100] G. D. Han, K. C. Neoh, K. Bae, H. J. Choi, S. W. Park, J.-W. W. Son, J. H. Shim, *J. Power Sources* **2016**, *306*, 503.
- [101] G. D. Han, H. J. H. R. Choi, K. Bae, H. J. H. R. Choi, D. Y. Jang, J. H. Shim, *ACS Appl. Mater. Interfaces* **2017**, *9*, 39347.
- [102] G. D. Han, K. Bae, E. H. Kang, H. J. Choi, J. H. Shim, *ACS Energy Lett.* **2020**, *5*, 1586.
- [103] V. Esposito, C. Gadea, J. Hjelm, D. Marani, Q. Hu, K. Agersted, S. Rammousse, S. H. Jensen, *J. Power Sources* **2015**, *273*, 89.
- [104] C. Li, H. Shi, R. Ran, C. Su, Z. Shao, *Int. J. Hydrogen Energy* **2013**, *38*, 9310.
- [105] C. Li, H. Chen, H. Shi, M. O. Tade, Z. Shao, *J. Power Sources* **2015**, *273*, 465.
- [106] N. M. Farandos, L. Kleiminger, T. Li, A. Hankin, G. H. Kelsall, *Electrochim. Acta* **2016**, *213*, 324.
- [107] N. M. Farandos, T. Li, G. H. Kelsall, *Electrochim. Acta* **2018**, *270*, 264.
- [108] Z. Chen, J. Ouyang, W. Liang, Z. Chao Yan, F. Stadler, C. Lao, *Ceram. Int.* **2018**, *44*, 13381.
- [109] Z. Zhu, Z. Gong, P. Qu, Z. Li, S. A. Rasaki, Z. Liu, P. Wang, C. Liu, C. Lao, Z. Chen, *J. Adv. Ceram.* **2021**, *10*, 279.
- [110] A. M. Sureshini, R. Cummins, T. L. Reitz, R. M. Miller, *Electrochim. Solid-State Lett.* **2009**, *12*, B176.
- [111] D. Young, A. M. Sureshini, R. Cummins, H. Xiao, M. Rottmayer, T. Reitz, *J. Power Sources* **2008**, *184*, 191.
- [112] M. A. Sureshini, R. Cummins, T. L. Reitz, R. M. Miller, *J. Am. Ceram. Soc.* **2009**, *92*, 2913.
- [113] N. Faino, W. Rosensteel, B. Gorman, N. Sullivan, *ECS Trans.* **2011**, *35*, 593.
- [114] T. Y. Hill, T. L. Reitz, M. A. Rottmayer, H. Huang, *ECS J. Solid State Sci. Technol.* **2015**, *4*, P3015.
- [115] T. Y. Hill, T. L. Reitz, H. Huang, *Mater. Res. Bull.* **2016**, *84*, 437.
- [116] T. Hill, T. Reitz, H. Huang, *TechConnect Briefs* **2016**, *4*, 143.
- [117] S. H. Rahul, K. Balasubramanian, S. Venkatesh, *Int. J. Precis. Eng. Manuf.* **2015**, *16*, 2553.
- [118] S. H. Rahul, K. Balasubramanian, S. Venkatesh, *Mater. Today Proc.* **2015**, *2*, 3552.
- [119] S. H. Rahul, K. Balasubramanian, S. Venkatesh, *Ceram. Int.* **2017**, *43*, 4513.
- [120] S. Venkatesh, S. H. Rahul, K. Balasubramanian, *Ceram. Int.* **2020**, *46*, 3994.
- [121] R. I. I. Tomov, M. Krauz, J. Jewulski, S. C. C. Hopkins, J. R. R. Kluczowski, D. M. M. Glowacka, B. A. A. Glowacki, *J. Power Sources* **2010**, *195*, 7160.
- [122] C. Wang, S. C. Hopkins, R. I. Tomov, R. V. Kumar, B. A. Glowacki, *J. Eur. Ceram. Soc.* **2012**, *32*, 2317.

- [123] I. Van Driessche, S. Hopkins, P. Lommens, X. Granados, D. Andreouli, B. Glowacki, I. M. Arabatzis, M. Arin, S. Ricart, I. Fasaki, E. Georgiopoulos, R. Tomov, *Nanosci. Nanotechnol. Lett.* **2013**, *5*, 466.
- [124] M. Dudek, R. I. Tomov, C. Wang, B. A. A. Glowacki, P. Tomczyk, R. P. P. Socha, M. Mosiałek, *Electrochim. Acta* **2013**, *105*, 412.
- [125] R. I. Tomov, A. Fakeeh, V. V. Krishnan, K. Balasubramanian, V. R. Kumar, B. A. Glowacki, *ECS Trans.* **2015**, *68*, 2491.
- [126] R. I. Tomov, M. Dudek, S. C. Hopkins, M. Krauz, H. Wang, C. Wang, Y. Shi, P. Tomczyk, B. A. Glowacki, *ECS Trans.* **2013**, *57*, 1359.
- [127] R. I. Tomov, M. Krauz, A. Tluczek, R. Kluczewski, V. V. Krishnan, K. Balasubramanian, R. V. Kumar, B. A. Glowacki, *Mater Renew Sustain Energy* **2015**, *4*, 14.
- [128] R. I. Tomov, R. Duncan, M. Krauz, R. Vasant Kumar, B. A. Glowacki, *E3S Web Conf.* **2016**, *10*, 00098.
- [129] C. Wang, R. I. Tomov, T. B. Mitchell-Williams, R. V. Kumar, B. A. Glowacki, *J. Appl. Electrochem.* **2017**, *47*, 1227.
- [130] R. I. Tomov, T. Mitchell-Williams, C. Gao, R. V. Kumar, B. A. Glowacki, *J. Appl. Electrochem.* **2017**, *47*, 641.
- [131] B. Shri Prakash, S. Senthil Kumar, S. T. Aruna, *Renewable Sustainable Energy Rev.* **2014**, *36*, 149.
- [132] Y. Rho, K.-T. Kang, D. Lee, *Nanoscale* **2016**, *8*, 8976.
- [133] L. J. Deiner, K. A. Piotrowski, T. L. Reitz, *J. Am. Ceram. Soc.* **2013**, *96*, 750.
- [134] K. Kamlungsua, T.-H. Lee, S. Lee, P.-C. Su, Y.-J. Yoon, *Int. J. Hydrogen Energy* **2021**, *46*, 30853.
- [135] J. A. Darr, J. Zhang, N. M. Makwana, X. Weng, *Chem. Rev.* **2017**, *117*, 11125.
- [136] M. Yoshimura, T. Hiuga, S. Sōmiya, *J. Cryst. Growth* **1985**, *71*, 277.
- [137] X. Weng, D. Brett, V. Yufit, P. Shearing, N. Brandon, M. Reece, H. Yan, C. Tighe, J. A. Darr, *Solid State Ionics* **2010**, *181*, 827.
- [138] Y. B. Khollam, A. S. Deshpande, A. J. Patil, H. S. Potdar, S. B. Deshpande, S. K. Date, *Mater. Chem. Phys.* **2001**, *71*, 235.
- [139] N. M. Islam, T. Noguchi, Y. Hakuta, H. Hayashi, *Nanosci. Nanotechnol. Lett.* **2011**, *3*, 324.
- [140] S. Hong, D. Lee, H. Yang, Y.-B. Kim, *Appl. Surf. Sci.* **2018**, *444*, 430.
- [141] G. Dell'Agli, L. Spiridigliozzi, A. Marocco, G. Accardo, C. Ferone, R. Cioffi, *J. Appl. Biomater. Funct. Mater.* **2016**, *14*, 189.
- [142] L. M. P. Garcia, D. A. Macedo, G. L. Souza, F. V. Motta, C. A. Paskocimas, R. M. Nascimento, *Ceram. Int.* **2013**, *39*, 8385.
- [143] S. Y. Lee, J. Yun, W.-P. Tai, *Adv. Powder Technol.* **2018**, *29*, 2423.
- [144] Y. Xu, N. Farandos, M. Rosa, P. Zielke, V. Esposito, P. Vang Hendriksen, S. H. Jensen, T. Li, G. Kelsall, R. Kiebach, *Int. J. Appl. Ceram. Technol.* **2018**, *15*, 315.
- [145] M. Rosa, P. N. N. Gooden, S. Butterworth, P. Zielke, R. Kiebach, Y. Xu, C. Gadea, V. Esposito, *J. Eur. Ceram. Soc.* **2019**, *39*, 2.
- [146] M. Rosa, P. Zielke, R. Kiebach, V. C. Bassetto, A. Lesch, V. Esposito, *J. Eur. Ceram. Soc.* **2019**, *39*, 1279.
- [147] P. Zielke, Y. Xu, S. B. Simonsen, P. Norby, R. Kiebach, *J. Supercrit. Fluids* **2016**, *117*, 1.
- [148] P. J. Blood, J. P. Denyer, B. J. Azzopardi, M. Poliakoff, E. Lester, *Chem. Eng. Sci.* **2004**, *59*, 2853.
- [149] E. H. Da'as, J. T. S. Irvine, E. Traversa, S. Bouffrad, *ECS Trans.* **2013**, *57*, 1851.
- [150] E. Venezia, M. Viviani, S. Presto, V. Kumar, R. I. Tomov, *Nanomaterials* **2019**, *9*, 654.
- [151] T. B. Mitchell-Williams, R. I. Tomov, S. A. Saadabadi, M. Krauz, P. V. Aravind, B. A. Glowacki, R. V. Kumar, *Mater. Renewable Sustainable Energy* **2017**, *6*, 12.
- [152] M. Kim, D. H. Kim, G. D. Han, H. J. Choi, H. R. Choi, J. H. Shim, *J. Alloys Compd.* **2020**, *843*, 155806.
- [153] C. Wang, R. I. Tomov, R. V. Kumar, B. A. Glowacki, R. Vasant Kumar, B. A. Glowacki, R. V. Kumar, B. A. Glowacki, *J. Mater. Sci.* **2011**, *46*, 6889.
- [154] O. Rahumi, A. Sobolev, M. K. Rath, K. Borodianskiy, *J. Eur. Ceram. Soc.* **2021**, *41*, 4528.
- [155] C. Gadea, Q. Hanniet, A. Lesch, D. Marani, S. H. Jensen, V. Esposito, *J. Mater. Chem. C* **2017**, *5*, 6021.
- [156] G. Perin, C. Gadea, M. Rosa, S. Sanna, Y. Xu, R. Kiebach, A. Glisenti, V. Esposito, *J. Phys. Chem. Solids* **2019**, *132*, 162.
- [157] H. Shimada, F. Ohba, X. Li, A. Hagiwara, M. Ihara, *J. Electrochem. Soc.* **2012**, *159*, F360.
- [158] E. Napadensky, *Chemistry of Inkjet Inks*, World Scientific, Singapore **2009**, pp. 255–267.
- [159] A. Kamyshny, S. Magdassi, *Nanomaterials in 2D and 3D Printing*, Wiley-VCH, Weinheim, Germany **2017**, pp. 119–160.
- [160] Y. H. Yun, J. D. Kim, B. K. Lee, Y. W. Cho, H. Y. Lee, *Macromol. Res.* **2009**, *17*, 197.
- [161] E. A. Clark, M. R. Alexander, D. J. Irvine, C. J. Roberts, M. J. Wallace, S. Sharpe, J. Yoo, R. J. M. Hague, C. J. Tuck, R. D. Wildman, *Int. J. Pharm.* **2017**, *529*, 523.
- [162] C. Xu, W. Chai, Y. Huang, R. R. Markwald, *Biotechnol. Bioeng.* **2012**, *109*, 3152.
- [163] E. Ruiz-Trejo, A. Atkinson, N. P. Brandon, *J. Power Sources* **2015**, *280*, 81.
- [164] B. Song, E. Ruiz-Trejo, N. P. Brandon, *J. Power Sources* **2018**, *395*, 205.
- [165] S. Pandiyan, A. El-Kharouf, R. Steinberger-Wilckens, *J. Colloid Interface Sci.* **2020**, *579*, 82.
- [166] E. H. Da'as, L. Bi, S. Bouffrad, E. Traversa, *Sci. China Mater.* **2018**, *61*, 57.
- [167] J. S. Park, H. J. Choi, G. D. Han, J. Koo, E. H. Kang, D. H. Kim, K. Bae, J. H. Shim, *J. Power Sources* **2021**, *482*, 229043.



**Leila Zouridi** holds a Bachelor's degree in Chemistry and a Master's degree in Materials Science. She is currently a Ph.D. candidate at the Materials Science and Technology department at the University of Crete. Her Ph.D. thesis focuses on the additive manufacturing of both hydrogen fueled solid oxide fuel cells and hydrogen gas sensing devices. Her current research interests lie on solution-based and mechanochemical synthesis, crystalline structure and properties of nanomaterials, ink development, printing of thin films, thermochromic coatings, and sustainable energy applications (solid oxide fuel cells and hydrogen technology).



**Ioannis Garagounis** completed his diploma and Ph.D. in Chemical Engineering at Aristotle University of Thessaloniki under the supervision of Prof. Michael Stoukides. His Ph.D. focused on developing anodes for direct carbon fuel cells. He is currently a postdoctoral researcher at CPERI/CERTH and the Department of Chemical Engineering of the University of Western Macedonia. He has worked on various aspects of heterogeneous catalysis and solid state electrochemistry. His research focuses on developing electrodes for ammonia synthesis/decomposition and CO<sub>2</sub> electrohydrogenation in solid electrolyte cells, as well as on direct biomass fuel cells.



**Anastasios Vourros** completed his diploma in Chemical Engineering (2013), followed by Ph.D. (2019) under the supervision of Prof. Michael Stoukides at Aristotle University of Thessaloniki. His Ph.D. focused on developing cathodes for electrochemical ammonia synthesis cells, culminating in an electrochemical Haber–Bosch process. He is currently a postdoctoral researcher at CPERI/CERTH. His current research interests include electrochemical ammonia synthesis and decomposition in solid electrolyte cells, CO<sub>2</sub> electrolysis, and hydrogenation cells, as well as steam electrolysis and direct biomass fuel cells.



**George E. Marnellos** holds a bachelor and a Ph.D. degree in Chemical Engineering from the Aristotle University of Thessaloniki, Greece. He is currently a professor in the Department of Mechanical Engineering at the University of Western Macedonia, Greece. Based on his background in heterogeneous catalysis, solid state electrochemistry, and thermochemical process engineering, his research activities are lying on energy conversion and storage technologies (P2X), hydrocarbons processing, hydrogen (reforming, electrolysis) and fuel cell (SOFCs, hybrid DFCs) technologies, CO<sub>2</sub> utilization (hydrogenation, electrolysis), air pollution control (NO<sub>x</sub>, VOCs, etc.), and bioenergy technologies.



**Vassilios Binas** is an associate researcher at IESL/FORTH and visiting professor at Department of Physics of UoC. He holds a Ph.D. degree from University of Crete (2010), with the dissertation “Synthesis and Characterization of Novel Nanoporous materials for Adsorption and Catalytic applications.” His research interests focus on physicochemical properties of advanced materials and devices for environmental and energy applications. Particular emphasis is given on heterogeneous catalysis for solar driven water splitting/CO<sub>2</sub> conversion and on printable electrochemical devices (SOFCs, gas sensors, supercapacitors, etc.).